BEILSTEIN JOURNAL OF NANOTECHNOLOGY

Innovative nanomaterials for next-generation bio- and chemosensing

Edited by Thanh-Danh Nguyen, Duong Tuan Quang and Olga Guliy

Imprint

Beilstein Journal of Nanotechnology
www.bjnano.org
ISSN 2190-4286
Email: journals-support@beilstein-institut.de

The *Beilstein Journal of Nanotechnology* is published by the Beilstein-Institut zur Förderung der Chemischen Wissenschaften.

Beilstein-Institut zur Förderung der Chemischen Wissenschaften
Trakehner Straße 7–9
60487 Frankfurt am Main
Germany
www.beilstein-institut.de

BEILSTEIN JOURNAL OF NANOTECHNOLOGY

Electrochemical sensing of sildenafil in pharmaceutical formulations using an (S,N)-doped reduced graphene oxide-modified electrode

Nguyen Quang Man[1], Ngo Thi Thanh Xuan[*2,3], Vo Thi Khanh Ly[1], Le Van Thanh Son[4], Le Duc Anh[5], Le Thi Hong Phong[6], Nguyen Hai Phong[2], Pham Khac Lieu[2], Le Lam Son[*2] and Dinh Quang Khieu[*2]

Full Research Paper

Open Access

Address:
[1]University of Medicine and Pharmacy, Hue University, 530000, Vietnam, [2]University of Sciences, Hue University, 530000, Vietnam, [3]Drug, Cosmetic, and Food Quality Control Center of Hue city, 530000, Vietnam, [4]University of Education and Science, The University of Danang, 550000, Vietnam, [5]Viet Nam National Institute of Occupational Safety and Health, Hanoi, Vietnam and [6]Institute of Materials Sciences, Vietnam Academy of Science and Technology, 18 Hoang Quoc Viet, Cau Giay, Hanoi City, 100000, Vietnam

Email:
Ngo Thi Thanh Xuan* - thanhxuanknh@gmail.com;
Le Lam Son* - lelamson@hueuni.edu.vn;
Dinh Quang Khieu* - dqkhieu@hueuni.edu.vn

* Corresponding author

Keywords:
differential pulse voltammetry; electrode modifier; rGO; (S,N)-rGO; sildenafil

Beilstein J. Nanotechnol. **2026,** *17,* 1087–1102.
https://doi.org/10.3762/bjnano.17.74

Received: 20 May 2026
Accepted: 22 July 2026
Published: 11 August 2026

This article is part of the thematic issue "Innovative nanomaterials for next-generation bio- and chemosensing".

Guest Editor: O. Guliy

Abstract

In this work, (S,N)-co-doped reduced graphene oxide ((S,N)-rGO) was successfully synthesized via thermal treatment and thoroughly characterized by X-ray diffraction, high-resolution transmission electron microscopy, elemental mapping, photoluminescence, and Raman spectroscopy, confirming the successful incorporation of nitrogen and sulfur into the graphene framework. The obtained (S,N)-rGO was used to modify a glassy carbon electrode for the electrochemical determination of sildenafil (SDN). The modified electrode exhibited enhanced electrocatalytic activity toward SDN oxidation, providing a well-defined current response. Under optimized conditions, the sensor showed a good linear relationship between peak current and SDN concentration in the range of 0.25–4.98 μM, with a low limit of detection of 0.24 μM and a limit of quantification of 0.78 μM. The proposed sensor demonstrated satisfactory repeatability, reproducibility, and stability, as well as good selectivity in the presence of potential interfering substances. The applicability of the method was validated by the determination of SDN in pharmaceutical samples. The results were in good agreement with those from high-performance liquid chromatography, indicating that the proposed electrochemical method is reliable and suitable for practical analysis.

Introduction

Sildenafil (SDN) is a widely prescribed phosphodiesterase type 5 (PDE-5) inhibitor used for the treatment of erectile dysfunction and pulmonary arterial hypertension. Its pharmacological activity is based on the selective inhibition of PDE-5, which increases the intracellular level of cyclic guanosine monophosphate (cGMP), resulting in smooth muscle relaxation and vasodilation. Phosphodiesterase-5 inhibitors, including SDN, are considered first-line therapeutic agents and have demonstrated significant efficacy in improving vascular function and clinical outcomes [1]. Furthermore, these agents enhance nitric oxide-mediated signaling pathways, thereby promoting increased blood flow in vascular tissues [2]. The widespread clinical use of SDN has led to a substantial increase in global consumption, which is accompanied by growing concerns regarding its misuse and illegal adulteration. Recent studies have reported that PDE-5 inhibitors are frequently detected as undeclared active ingredients in dietary supplements and counterfeit pharmaceutical products marketed as "natural" remedies [3]. This situation poses a serious public health risk as such products often evade regulatory control and may contain unpredictable or excessive dosages.

To date, various analytical techniques have been developed for the determination of SDN. Conventional methods such as gas chromatography/mass spectrometry (GC/MS) [4], liquid chromatography–tandem mass spectrometry (LC–MS/MS) [5], and high-performance liquid chromatography (HPLC) [6,7] are widely employed because of their high accuracy and sensitivity. In addition, advanced spectroscopic and hybrid approaches, including surface-enhanced Raman scattering (SERS) using Ag/UiO-66-decorated porous structures [8], thin-layer chromatography coupled with UV–SERS detection (TLC–UV–SERS) [9], dual-labeled probe time-resolved fluorescence immunochromatography assay [10], and fluorescence-based methods [11], have also been reported. Despite their excellent analytical performance, these techniques generally require sophisticated instrumentation, complex sample preparation, and relatively long analysis time.

In this context, electrochemical sensing has emerged as a promising alternative for SDN determination due to its inherent advantages, including operational simplicity, rapid response, low cost, and high sensitivity [12,13]. These features make electrochemical methods particularly suitable for on-site monitoring and routine analysis [14,15]. Importantly, the electrochemical oxidation of SDN can be effectively enhanced by tailoring the electrode surface with functional nanomaterials, thereby improving both sensitivity and selectivity.

Among various nanomaterials, graphene-based materials, especially reduced graphene oxide (rGO), have attracted considerable attention as electrode modifiers due to their excellent electrical conductivity, large specific surface area, and favorable electrocatalytic properties [16,17]. However, pristine rGO still suffers from a limited number of active sites and insufficient selectivity toward specific analytes. To overcome these limitations, heteroatom doping has been proposed as an effective strategy to modulate the electronic structure and enhance catalytic activity [18,19]. In particular, nitrogen and sulfur co-doping has been demonstrated to significantly improve electrochemical performance by introducing defects, redistributing charge density, and facilitating electron transfer processes [20,21].

In our previous study [22], nitrogen- and sulfur-doped reduced graphene oxide ((S,N)-rGO) was explored as a potential electrode modifier for the electrochemical detection of SDN, showing promising electrocatalytic behavior. However, that work was mainly limited to a proof-of-concept study and lacked a systematic investigation of the sensing mechanism, optimization of experimental conditions, and a comprehensive evaluation of analytical performance. Although various electrochemical sensors have been reported for SDN determination, many of them rely on multicomponent nanocomposites, noble-metal nanoparticles, or relatively complicated fabrication procedures. In contrast, the proposed (S,N)-rGO-modified electrode is prepared through a simple and facile synthesis strategy while providing enhanced electrocatalytic activity arising from the synergistic effects of nitrogen and sulfur co-doping. Together with its satisfactory analytical performance and successful application to pharmaceutical formulations, these features constitute the main novelty and practical advantage of the present work. To address these limitations, the present study builds on our previous findings and develops a more systematic electrochemical sensing strategy. In this work, (S,N)-co-doped reduced graphene oxide ((S,N)-rGO) was synthesized via a facile thermal treatment using ammonium persulfate as a dual heteroatom precursor. Incorporating nitrogen and sulfur heteroatoms is expected to generate abundant active sites, enhance electron transfer kinetics, and improve adsorption affinity for SDN molecules. The synthesized material was used to modify a glassy carbon electrode (GCE) for electrochemical detection. The fabricated (S,N)-rGO/GCE sensor exhibited significantly enhanced electrocatalytic activity toward the oxidation of SDN, resulting in improved sensitivity and selectivity compared with the bare electrode. The effects of key experimental parameters, including pH, scan rate, and accumulation conditions, were systematically investigated to elucidate the sensing mechanism. Furthermore, the analytical performance of the proposed sensor

was thoroughly evaluated in terms of linear range, limit of detection, reproducibility, and stability. Finally, the practical applicability of the method was demonstrated by determining SDN in real pharmaceutical samples, with satisfactory accuracy and recovery.

Experimental

Chemicals

Graphite powder, phosphoric acid (H_3PO_4, 85%), sulfuric acid (H_2SO_4, 98%), hydrochloric acid (HCl, 37%), potassium permanganate ($KMnO_4$, 99%), thiourea (CH_4N_2S, 99%), and hydrogen peroxide (H_2O_2, 30%) were obtained from Merck. Boric acid (H_3BO_3, 99.5%), phosphoric acid (H_3PO_4, 85%), acetic acid (CH_3COOH, 99.8%), and sodium hydroxide (NaOH, 98%) were purchased from Sigma-Aldrich and used for the preparation of Britton–Robinson (BR) buffer solutions with various pH values for electrochemical measurements. SDN citrate standard ($C_{28}H_{38}N_6O_{11}S$, 99%) was supplied by the National Institute of Drug Quality Control, Vietnam. All chemicals and reagents used throughout the study were of analytical grade and utilized without any further purification.

Apparatus

A conventional three-electrode system was used, consisting of a modified GCE as the working electrode, a platinum wire as the counter electrode, and an Ag/AgCl electrode as the reference electrode (CPA–HH5 Computerized Polarography Analyzer, Vietnam). Morphological and structural characterizations were performed using transmission electron microscopy (TEM) and energy-dispersive X-ray spectroscopy (EDX) mapping (JEM-2100, Jeol-Japan) at 200 kV, X-ray diffraction (XRD) (Bruker D8 Advance, Germany), Raman spectroscopy (XploRA™ PLUS, Horiba, Japan), FTIR (Shimadzu Prestige-21, Japan), and photoluminescence (PL) (Horiba Fluorolog 3 FL3-22 fluorometer).

Synthesis of graphene oxide

Graphene oxide (GO) was synthesized following a modified procedure based on the method reported by Diego C. Marcano and coworkers [23]. Briefly, 3 g of graphite powder was gradually added to a mixed acid solution containing 360 mL of concentrated H_2SO_4 and 40 mL of concentrated H_3PO_4 under continuous stirring. Subsequently, 18 g of $KMnO_4$ was slowly introduced into the mixture, resulting in a mildly exothermic reaction. The suspension was maintained under stirring for 72 h to allow for complete oxidation. Afterward, 17 mL of 30% H_2O_2 was added dropwise to terminate the reaction, and the mixture was allowed to cool to room temperature. The resulting product was separated by centrifugation at 5000 rpm for 15 min, and the supernatant was discarded to obtain a brownish-yellow solid. The solid was washed several times with 0.1 M HCl solution and deionized water to remove residual ions and impurities, followed by centrifugation. The purified material was then dried at 60 °C for 48 h to yield graphite oxide. This product was subsequently exfoliated by ultrasonic treatment in distilled water for 4 h. After centrifugation and drying at 60 °C for an additional 48 h, GO was obtained as a black solid.

Synthesis of (S,N)-doped graphene oxide ((S,N)-GO)

The synthesis of nitrogen and sulfur co-doped graphene oxide ((S,N)-GO) was carried out using a procedure similar to that described above. The key difference lies in the oxidation stage, where 1.5 g of thiourea was introduced into the reaction mixture immediately after the addition of $KMnO_4$, serving as a heteroatom dopant source.

Synthesis of (S,N)-doped reduced graphene oxide

To obtain reduced (S,N)-doped graphene oxide ((S,N)-rGO), 0.3 g of (S,N)-GO was dispersed in a mixture of 50 mL distilled water and 30 mL ethanol. The suspension was ultrasonicated for 60 min to ensure uniform dispersion, then transferred into a Teflon-lined autoclave. The hydrothermal reduction was conducted at 180 °C for 12 h. After naturally cooling to room temperature, the resulting black solid was collected by centrifugation, washed thoroughly with distilled water, and dried at 80 °C for 24 h. The final product was ground into a fine powder to obtain (S,N)-rGO.

Fabrication of the (S,N)-rGO-modified electrode

Prior to modification, the GCE surface was polished with an alumina slurry, thoroughly rinsed with deionized water, and sonicated sequentially in ethanol and water. A suspension of (S,N)-rGO (1 mg·mL^{-1}) was prepared by dispersing the material in water with ultrasonication. A defined volume of the suspension (5 µL) was drop-cast onto the cleaned GCE surface and dried at room temperature (≈30 min) to obtain the (S,N)-rGO/GCE.

Electrochemical measurements

The electrochemical behavior of SDN was investigated using cyclic voltammetry (CV) and differential pulse voltammetry (DPV) in a Britton–Robinson buffer solution at various pH values. Key experimental parameters, including accumulation potential, accumulation time, pulse amplitude, and scan rate, were optimized to achieve the best analytical performance. Calibration curves were constructed by measuring the peak current response at different concentrations of SDN. The limit of detection (LOD) and the limit of quantification (LOQ) were calcu-

lated based on the residual standard deviation of the calibration curve and its slope.

Sample preparation and analysis

Sample preparation

Ten SDN tablets were accurately weighed and the average tablet mass was determined. The tablets were then finely ground to obtain a homogeneous powder. An accurately weighed portion of the powder, equivalent to one tablet, was transferred into a 100 mL volumetric flask. Approximately 50 mL of distilled water was added, and the mixture was sonicated for 30 min to ensure complete extraction of SDN. The solution was then diluted to the mark with distilled water, thoroughly mixed, and filtered to obtain the stock sample solution. The obtained solution was further diluted with distilled water to an appropriate concentration depending on the SDN content in the pharmaceutical formulation (solution 1). An aliquot of solution 1 was then diluted with distilled water and Britton–Robinson buffer (0.1 M, pH 4.0) in the electrochemical cell to obtain a final SDN concentration of approximately 4.2 μM. The SDN content was determined using DPV with the standard addition technique.

Recovery study

For recovery evaluation, the prepared sample solution was diluted under the same conditions as described above. Subsequently, 20 μL of a 0.001 M SDN standard solution was added into a 20 mL electrochemical cell. The total SDN concentration was determined by DPV using the standard addition method. The original SDN content in the sample was subtracted, and the recovery was calculated by comparing the measured increase with the known added amount. All measurements were performed in triplicate. The recovery (%) was calculated according to the following equation:

$$\text{Recovery}(\%) = \frac{C_{\text{found}} - C_{\text{original}}}{C_{\text{added}}} \times 100$$

The relative standard deviation (RSD, %) was used to evaluate precision:

$$\text{RSD}(\%) = \frac{\text{SD}}{\text{mean}} \times 100$$

Results and Discussion

Characterization of materials

Figure 1 presents the characterization results for the obtained materials. The GO sample exhibits a characteristic diffraction peak at around 2θ ≈ 8.7°, corresponding to the (001) plane, indicating the presence of oxygen-containing functional groups and enlarged interlayer spacing [24]. After (S,N)-doping, the peak becomes broader and slightly shifted, suggesting partial disruption of the layered structure. For (S,N)-rGO, the disappearance of the GO peak and the emergence of a broad peak at ≈24.7° (002 plane) confirm the successful reduction process and partial restoration of graphitic domains [24]. The textural parameters in Table 1 and Figure 1b reveal a clear evolution of pore structure after doping and reduction. Pristine GO exhibits a very low BET surface area (6.93 $m^2 \cdot g^{-1}$) with no detectable microporosity, indicating a highly stacked structure with limited accessible surface. Upon (S,N)-co-doping, (S,N)-GO shows a significant increase in surface area (63.81 $m^2 \cdot g^{-1}$), mainly contributed by mesopores, suggesting that the introduction of heteroatoms and gas evolution during oxidation promotes exfoliation and pore formation. After reduction, rGO presents a hierarchical pore structure with both micropores (16.5 $m^2 \cdot g^{-1}$) and mesopores (43.8 $m^2 \cdot g^{-1}$). The formation of micropores can be attributed to the removal of oxygen-containing functional groups, which generates vacancy defects and creates nanoscale pores within the graphene sheets. Meanwhile, mesopores originate from the partial restacking and wrinkling of graphene layers. In contrast, (S,N)-rGO shows reduced microporous (13.1 $m^2 \cdot g^{-1}$) and mesoporous (29.6 $m^2 \cdot g^{-1}$) contributions compared to rGO. This decrease may result from structural rearrangement or partial pore collapse during hydrothermal treatment, as well as the occupation of pore sites by doped nitrogen and sulfur species.

The FTIR spectra (Figure 1c) confirm the successful oxidation and subsequent modification of GO. The broad band at ≈3400 cm^{-1} corresponds to O–H stretching vibrations, while peaks at ≈1728 cm^{-1} (C=O), ≈1619 cm^{-1} (C=C), and 1224–1053 cm^{-1} (C–O) are characteristic of oxygen-containing functional groups in GO [25]. After doping and reduction, the intensity of oxygen-related peaks decreases, indicating partial removal of oxygen functionalities [24]. New features observed at ≈1555 cm^{-1} and ≈1159 cm^{-1} suggest the incorporation of nitrogen- and sulfur-containing groups, confirming successful heteroatom. The Raman spectra (Figure 1d) display the typical D and G bands of graphene-based materials [26]. The I_D/I_G ratio increases from 0.82 (GO) to 1.21 ((S,N)-rGO), indicating an increase in structural defects and disorder after doping and reduction [27]. This increase is commonly attributed to the formation of smaller sp^2 domains and the introduction of defects by N and S heteroatoms. Such defects are beneficial for electrochemical applications, as they enhance electron transfer and provide more active sites. The combined results confirm that (S,N)-co-doping and reduction effectively modify the structural, textural, and electronic properties of GO, leading to enhanced electrochemical activity. These structural and surface modifications are expected to significantly improve the electrochemical performance of the (S,N)-rGO-modified electrode.

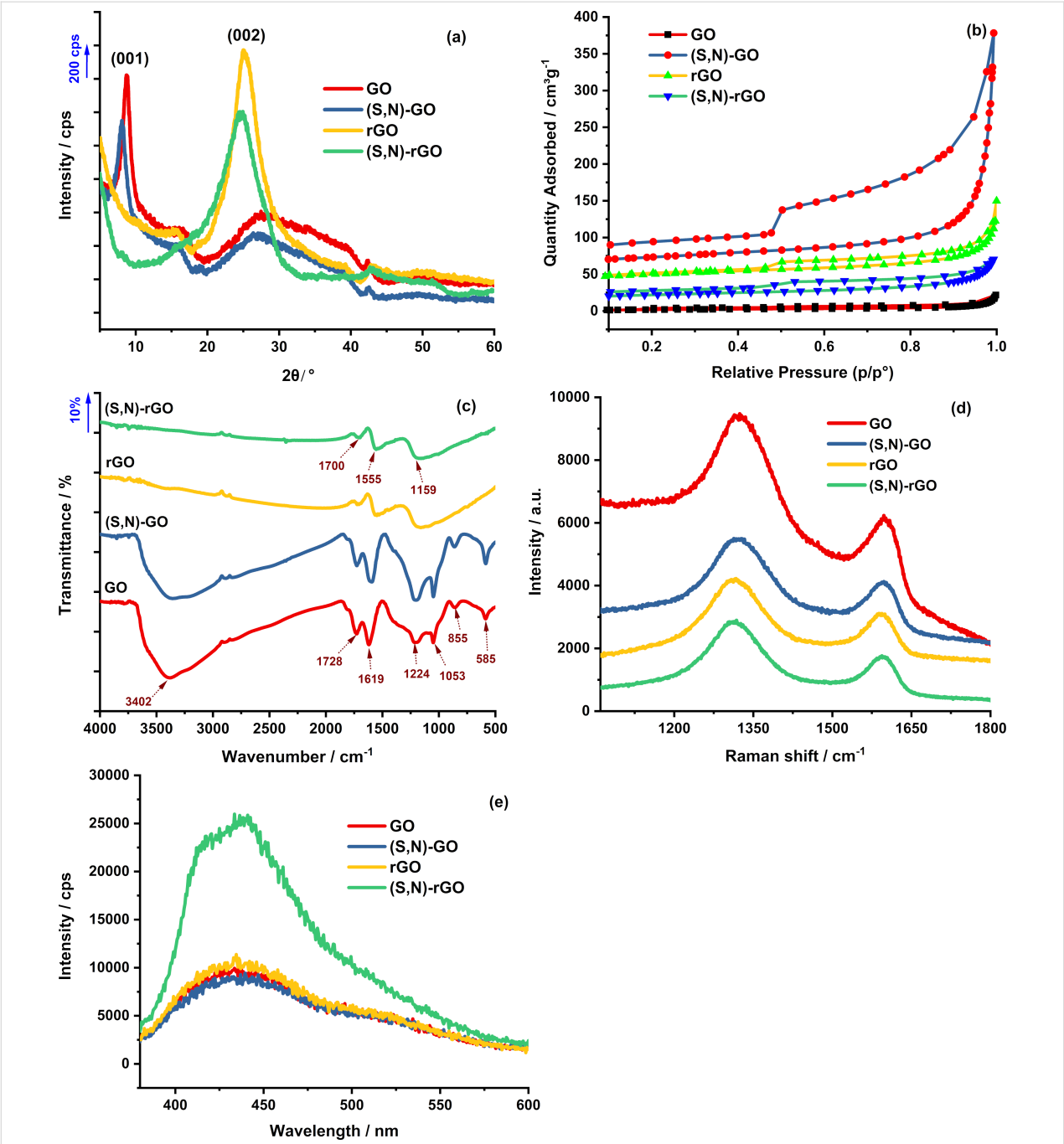

Figure 1: (a) XRD patterns, (b) nitrogen adsorption/desorption isotherms, (c) FTIR spectra, (d) Raman spectra, and (e) photoluminescence (PL) spectra of GO, (S,N)-GO, rGO and (S,N)-rGO.

Table 1: Textural properties and Raman intensity ratios (I_D/I_G) of GO, (S,N)-GO, rGO, and (S,N)-rGO.

Sample	BET ($m^2 \cdot g^{-1}$)	Micropores ($m^2 \cdot g^{-1}$)	Mesopores ($m^2 \cdot g^{-1}$)	I_D/I_G
GO	6.93	–	6.9	0.82
(S,N)-GO	63.81	–	63.8	0.98
rGO	60.31	16.5	43.8	1.05
(S,N)-rGO	42.63	13.1	29.6	1.21

The PL spectra of GO, (S,N)-GO, rGO, and (S,N)-rGO are shown in Figure 1e. All samples exhibit a broad emission band centered around 440–460 nm, which is commonly attributed to radiative recombination associated with oxygen-containing functional groups and defect states in graphene oxide-based materials. GO exhibits the highest PL intensity, indicating a high density of oxygenated defects that act as recombination centers for electron–hole pairs. After reduction and heteroatom doping, the PL intensity decreases significantly, especially for (S,N)-rGO. This quenching effect suggests the partial restoration of the conjugated sp^2 carbon network and improved charge mobility after removal of oxygen-containing groups. The reduced PL intensity of (S,N)-rGO indicates a lower recombination rate of charge carriers and more efficient electron transport capability. In addition, the incorporation of nitrogen and sulfur atoms can modify the electronic structure of graphene and introduce new electronic states, thereby facilitating charge-transfer processes. The PL results therefore further confirm the successful reduction and heteroatom functionalization of GO, in agreement with the XRD, FTIR, BET, and Raman analyses.

High-resolution transmission electron microscopy (HRTEM) images of (S,N)-GO and (S,N)-rGO are presented in Figure 2a and Figure 2b, respectively. The (S,N)-GO sample exhibits thin, transparent, and relatively smooth layered nanosheets with a typical wrinkled morphology characteristic of graphene oxide-based materials. The translucent appearance indicates the formation of few-layer graphene sheets with high exfoliation degree. After the reduction process, the morphology of (S,N)-rGO becomes more crumpled and corrugated, accompanied by partial restacking of graphene layers. The increased wrinkling and folding observed in Figure 2b can be attributed to the removal of oxygen-containing functional groups during reduction, which induces structural distortion and decreases electrostatic repulsion between graphene sheets. Such morphological changes are commonly observed in reduced graphene materials and indicate the partial restoration of the conjugated carbon network. Moreover, the highly wrinkled and defective structure of (S,N)-rGO is advantageous for electrochemical applications because it can prevent severe agglomeration of graphene sheets, expose more electroactive surface area, and facilitate electrolyte diffusion. The formation of folded nanosheet structures also creates abundant edge-plane-like defects and active sites, which are beneficial for electron-transfer reactions and analyte adsorption during electrochemical sensing.

The elemental mapping images and EDX spectrum of (S,N)-rGO are presented in Figure 3. The mapping results reveal the distribution of C, O, N, and S throughout the graphene framework, confirming the successful heteroatom functionalization of the reduced graphene oxide sheets. The strong carbon signal originates from the graphene backbone, while the oxygen signal indicates that a small amount of residual oxygen-containing functional groups remains after the reduction process. Notably, although the quantitative EDX analysis shows an extremely low nitrogen content (close to 0 atom %), the elemental mapping image still exhibits detectable N-related signals distributed over the graphene surface. This discrepancy can be attributed to the inherent limitation of EDX spectroscopy in quantitatively detecting light elements at ultralow concentrations. Because

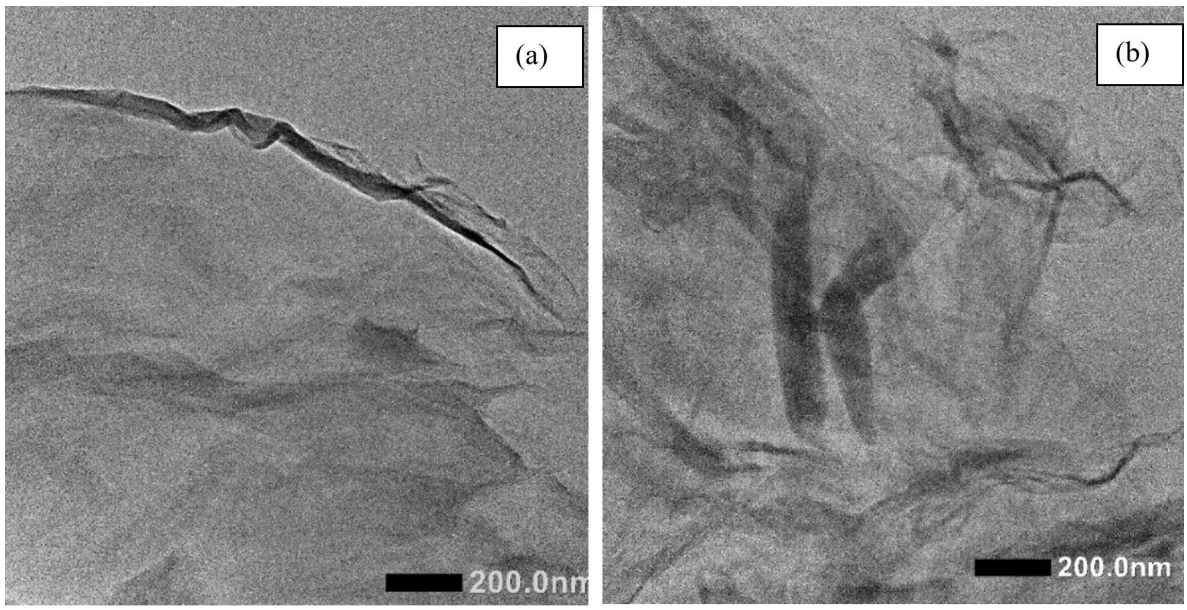

Figure 2: HRTEM observation of (S,N)-GO (a) and (S,N)-rGO (b).

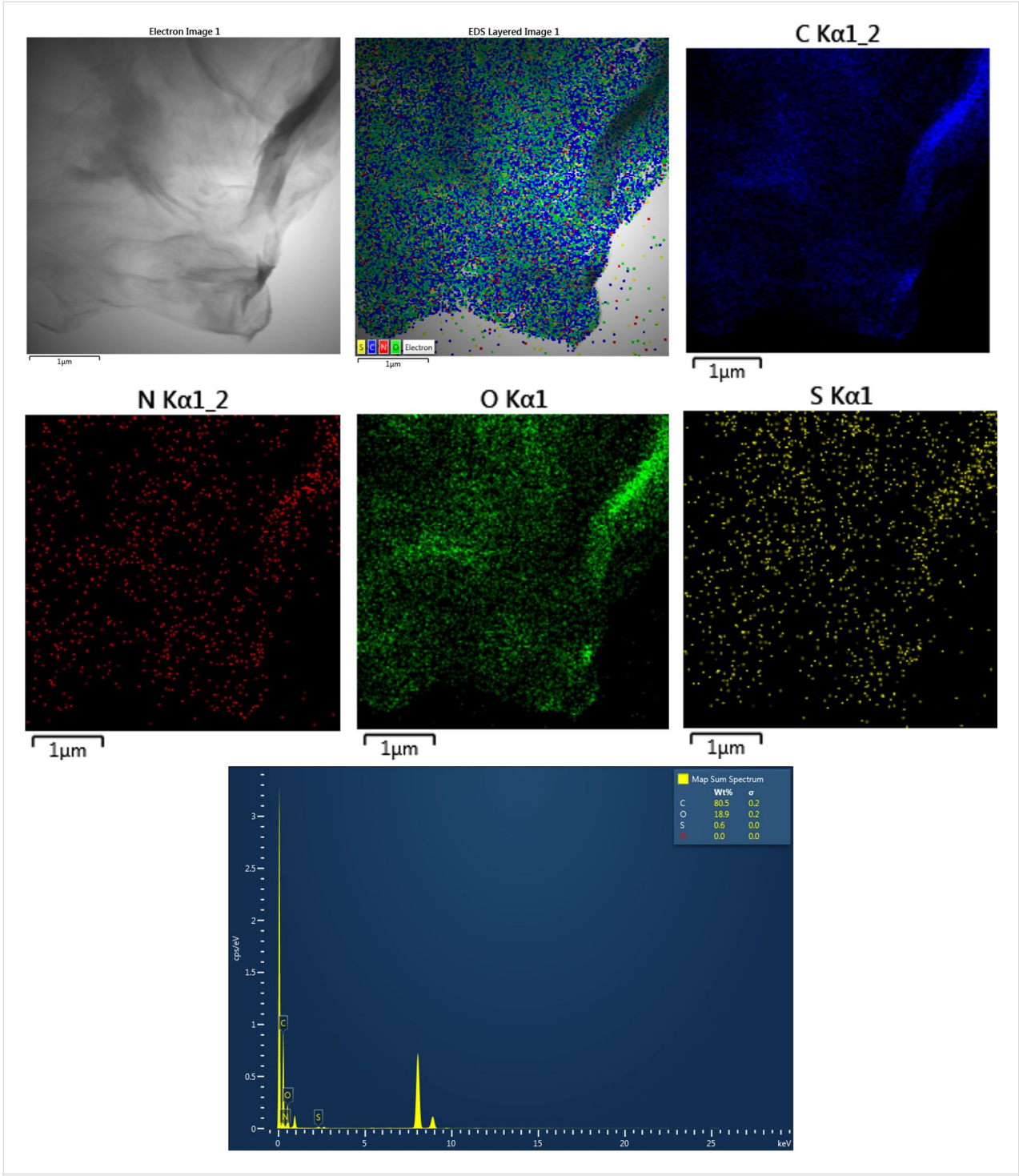

Figure 3: EDX mapping of (S,N)-rGO.

nitrogen has a low atomic number and weak X-ray emission intensity, its signal can easily fall below the reliable quantitative detection threshold, particularly in carbon-rich materials such as graphene derivatives [28,29]. Nevertheless, the mapping image qualitatively suggests the presence of trace nitrogen species distributed over the graphene surface. However, owing to the limited sensitivity of EDX for the quantitative analysis of light elements, particularly nitrogen in carbon-rich materials, this observation should be regarded as qualitative evidence rather than definitive proof of nitrogen incorporation. Therefore, the presence of nitrogen-containing species is suggested but cannot be conclusively confirmed by EDX alone. In contrast, sulfur

signals are more clearly observed and uniformly distributed across the graphene sheets, indicating more effective sulfur incorporation into the carbon framework.

Determination of SDN using a (S,N)-rGO modified electrode

Electrochemical behavior of SDN on different electrode

The electrochemical responses of SDN at different electrodes are presented in Figure 4a. The bare GCE exhibits a relatively weak oxidation current, indicating limited electron transfer kinetics. Upon modification with GO, the peak current increases slightly due to the larger surface area and presence of oxygen-containing functional groups. A more pronounced enhancement is observed for the (S,N)-GO/GCE, suggesting that heteroatom doping improves the electrical conductivity and introduces additional active sites for electron transfer. Notably, the (S,N)-rGO/GCE shows the highest current response, which can be attributed to the synergistic effect of (S,N)-co-doping and reduction. The reduction process restores the π-conjugated structure, facilitating faster electron transfer, while heteroatoms create defect sites that enhance electrocatalytic activity. As summarized in Figure 2b, the peak current increases in the order: GCE < GO/GCE < (S,N)-GO/GCE < rGO < (S,N)-rGO/GCE, confirming that the (S,N)-rGO-modified electrode exhibits the best electrochemical performance toward SDN detection.

The enhanced electrochemical response of the (S,N)-rGO/GCE can be attributed to the synergistic effects of reduced graphene oxide and nitrogen/sulfur heteroatom doping. The hydrothermal reduction restores the conjugated sp^2 carbon network, resulting in improved electrical conductivity and accelerated electron-transfer kinetics. Meanwhile, the incorporation of nitrogen and sulfur atoms introduces structural defects and heterogeneous electronic states, which act as additional electroactive sites for the oxidation of SDN. Nitrogen dopants increase the electron density of adjacent carbon atoms, whereas sulfur dopants induce charge polarization and further modulate the local electronic structure. These heteroatom-induced effects facilitate charge transfer across the electrode/electrolyte interface and lower the activation energy for the oxidation reaction. Furthermore, the aromatic structure of SDN can interact with the π-conjugated graphene surface through π–π stacking interactions, while residual oxygen-containing functional groups and heteroatom sites may promote adsorption through hydrogen bonding and electrostatic interactions. Consequently, the combination of improved conductivity, increased density of active sites, and enhanced adsorption affinity results in the significantly higher oxidation current observed at the (S,N)-rGO-modified electrode.

Effect of the pH value

The effect of pH on the electrochemical response of SDN at the (S,N)-rGO/GCE was investigated over the pH range of 2.0–8.0 (Figure 5a). The oxidation peak current initially increased with increasing pH, reached a maximum at pH 4.0, and then gradually decreased at higher pH values (Figure 5b). The oxidation peak current initially increased with increasing pH, reached a maximum at pH 4.0, and then gradually decreased at higher pH values (Figure 5b). During the pH study, only a single oxidation peak of SDN was observed in the pH range of 2.0–5.0. However, at pH 6.0–8.0, an additional oxidation peak appeared adjacent to the main SDN oxidation peak, which is likely associated with the formation of oxidation and/or degradation prod-

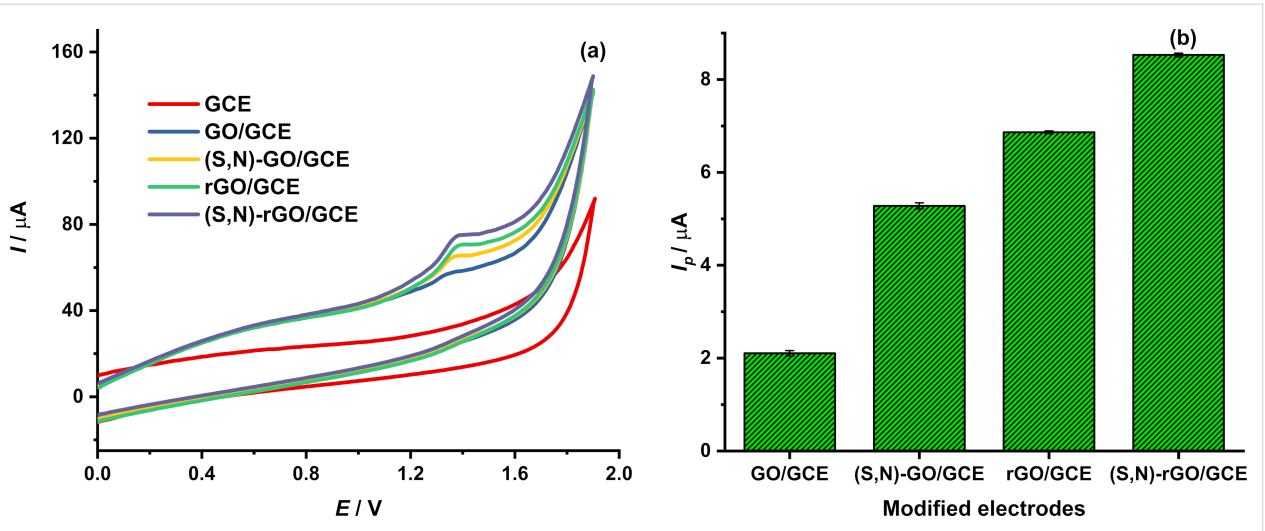

Figure 4: (a) Cyclic voltammograms (CVs) recorded at different electrodes (GCE, GO/GCE, (S,N)-GO/GCE, rGO/GCE and (S,N)-rGO/GCE) in 0.1 M BR buffer (pH 3.0) containing 20 μM SDN at a scan rate of 0.2 $V \cdot s^{-1}$; (b) corresponding peak currents obtained at different electrodes (n = 3).

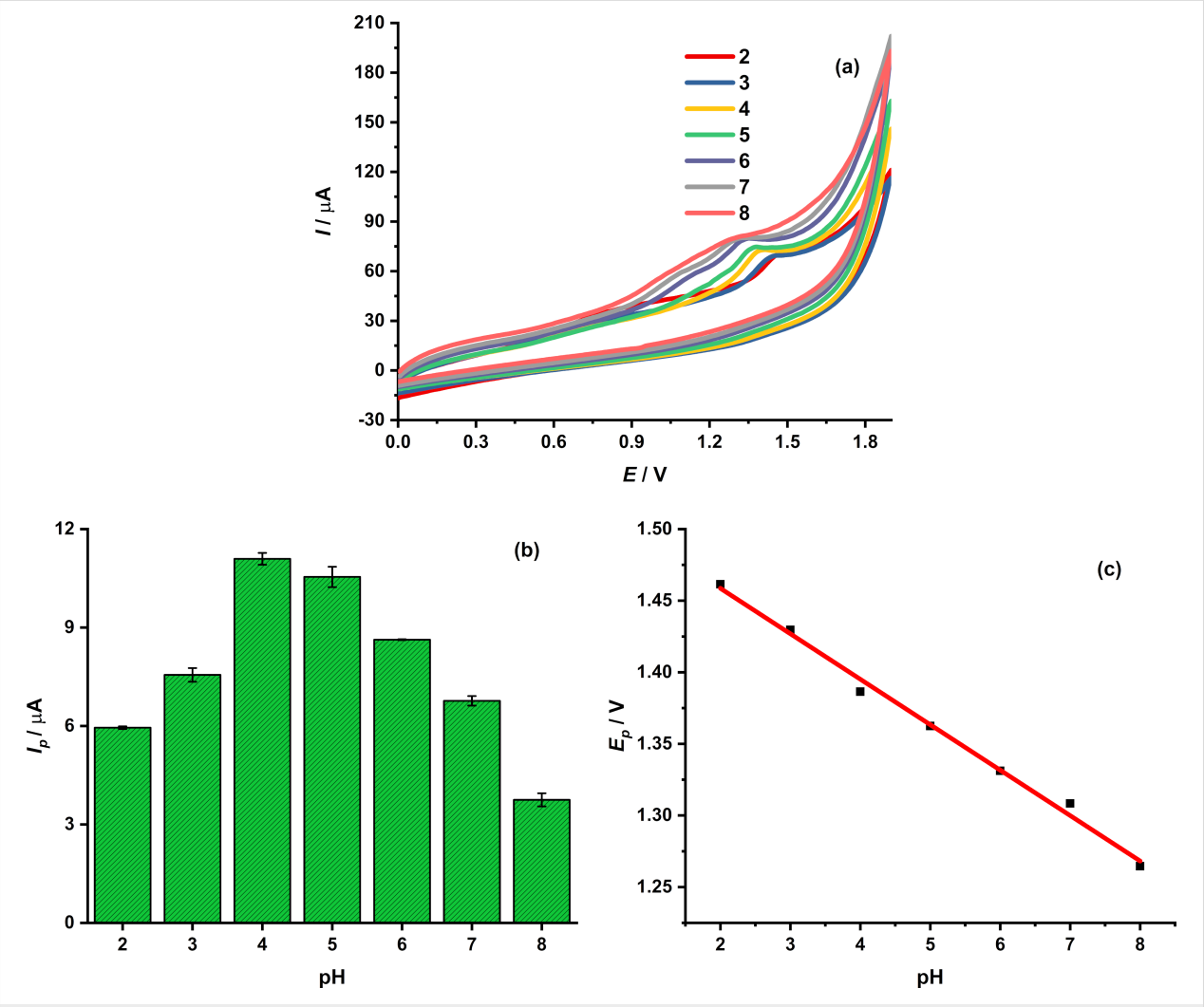

Figure 5: (a) CVs of (S,N)-rGO/GCE in 0.1 M Britton–Robinson buffer at different pH values (2.0–8.0) containing 20 μM SDN at a scan rate of 0.2 V·s^{-1}; (b) variation of anodic peak current with pH; (c) dependence of peak potential (E_p) on pH.

ucts. Consequently, the CV curves in Figure 5a represent the overall anodic response, whereas the quantitative values shown in Figure 5b were obtained by integrating only the main SDN oxidation peak using Origin software. The contribution of the additional oxidation peak was intentionally excluded from the quantitative analysis. Therefore, although the overall anodic current appears higher at pH 6.0–8.0, the current corresponding solely to the main SDN oxidation peak decreases, resulting in lower peak currents than those observed at pH 4.0 and 5.0. These results indicate that proton participation plays an important role in the electrochemical oxidation of SDN, and therefore pH 4.0 was selected as the optimum supporting electrolyte for subsequent experiments.

As shown in Figure 5c, the oxidation peak potential shifted linearly toward less positive values with increasing pH, following the equation:

$$E_{SDN} = (1.5221 \pm 0.0061) + (-0.0317 \pm 0.0011)\,\text{pH};$$
$$r^2 = 0.9937.$$

The slope of 0.0317 V·pH^{-1} is close to half of the theoretical Nernstian value of 0.059 V·pH^{-1}, suggesting that the number of protons involved in the electrochemical oxidation process is lower than the number of transferred electrons. Based on the Nernst relationship, the proton-to-electron ratio can be estimated to be approximately 0.5, indicating that the number of electrons participating in the oxidation process is likely twice that of protons. However, it should be noted that the reported pH dependence for SDN oxidation varies considerably in the literature. A study [30] has reported slopes close to the theoretical Nernstian value of 0.059 V·pH^{-1}, indicating an equal number of protons and electrons participating in the reaction, where-

as other [31] has described slopes near half of this theoretical value, corresponding to a proton-to-electron ratio of approximately 1:2. These discrepancies may arise from differences in electrode materials, surface interactions, and oxidation mechanisms. In the present study, the observed deviation may be attributed to the strong electronic interaction between SDN and the conductive (S,N)-rGO surface, together with possible adsorption effects and multistep oxidation pathways occurring at the electrode interface.

Scan rate effect

The effect of scan rate on the electrochemical behavior of SDN at the (S,N)-rGO/GCE was investigated in the range of 0.07–0.40·V s^{-1} (Figure 6a). The oxidation peak current increased with increasing scan rate, indicating enhanced mass transport toward the electrode surface. As shown in Figure 6b, the peak current exhibited a good linear relationship with the square root of scan rate:

$$I_{SDN} = (0.0802 \pm 0.1463) + (18.0462 \pm 0.3175)\nu^{1/2};$$
$$r^2 = 0.9978.$$

This result indicates that the electrochemical oxidation process is predominantly diffusion-controlled. Further insight was obtained from the log–log relationship (Figure 6c):

$$\log I_{SDN} = (1.2554 \pm 0.0056) + (0.4921 \pm 0.0070)\log \nu;$$
$$r^2 = 0.9986.$$

The slope value (≈0.49) is very close to the theoretical value of 0.5 expected for a diffusion-controlled process, further confirming that diffusion is the dominant transport mechanism. Nevertheless, considering the high surface area and π-electron-rich structure of (S,N)-rGO, surface interaction and partial adsorption of SDN on the electrode surface may also contribute to the overall electrochemical response.

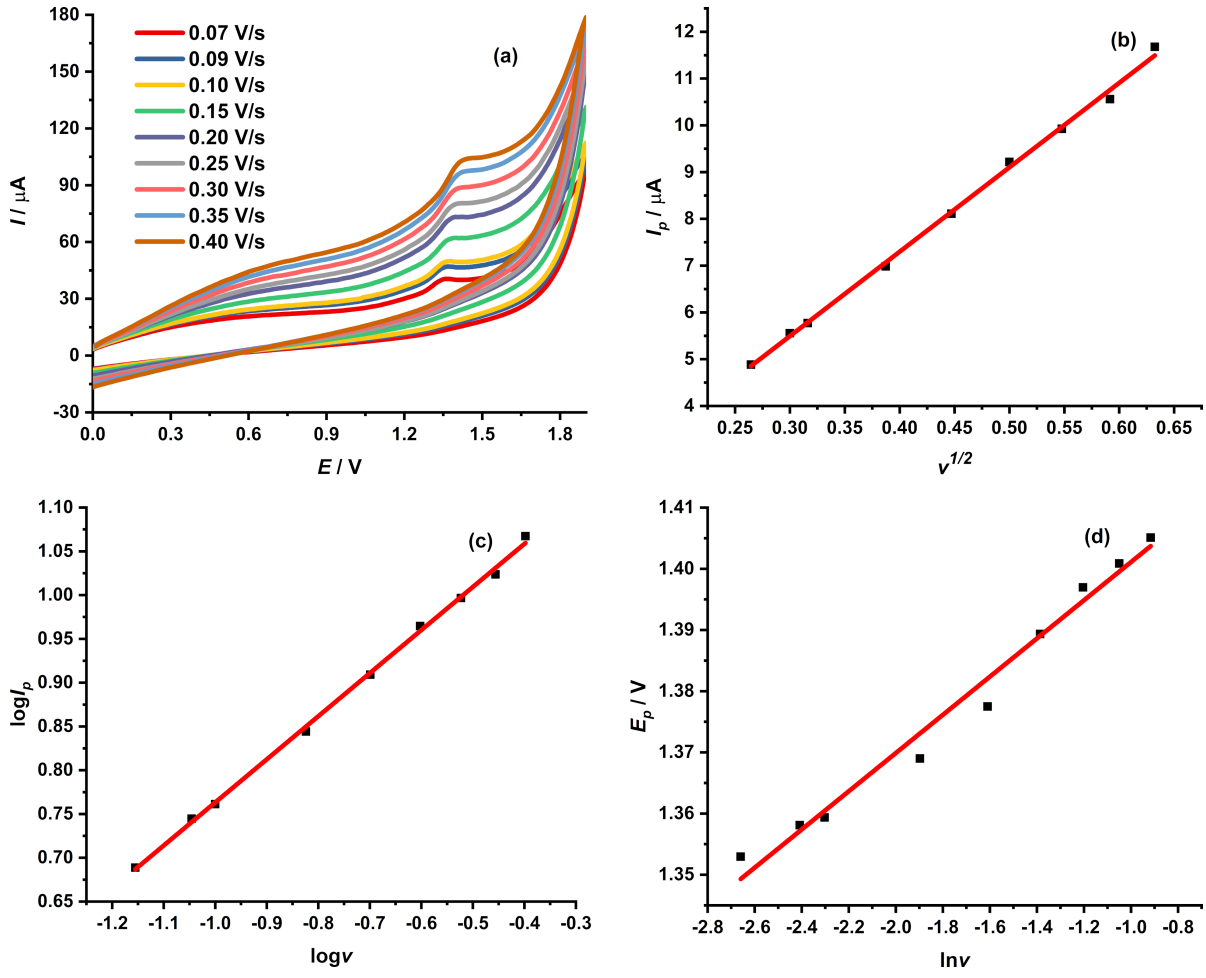

Figure 6: (a) CVs of (S,N)-rGO/GCE in 0.1 M Britton–Robinson buffer (pH 4.0) containing 20 μM SDN at different scan rates (0.07–0.40 V s^{-1}); (b) linear relationship between peak current (I_p) and the square root of scan rate ($v^{1/2}$); (c) linear plot of log I_p versus log v; (d) dependence of peak potential (E_p) on ln v.

For an irreversible electrochemical process, the relationship between peak potential and scan rate is described by the Laviron equation (Figure 6d):

$$E_{SDN} = (1.4323 \pm 0.0030) + (0.0312 \pm 0.00166) \ln \nu;$$
$$r^2 = 0.9807.$$

According to Laviron theory [32]:

$$\text{slope} = RT/\alpha nF$$

(R: molar gas constant (8.314 J·mol^{-1}·K^{-1}); T: the absolute temperature (K); α: the electron-transfer coefficient; n: the number of transferred electrons; F: the Faraday constant (96485 C·mol^{-1}). At 25 °C (RT/F ≈ 25.7 mV), the slope value of 0.0312 V gives: αn = 0.0257/0.0312 ≈ 0.823.

Assuming a typical transfer coefficient of α ≈ 0.5 for an irreversible process [33]:

$$n = 0.823/0.5 \approx 1.65 \approx 2.$$

Thus, the electrooxidation of SDN involves approximately two electrons. Although the exact molecular oxidation mechanism of SDN could not be conclusively established in the present work, the combined pH dependence, scan-rate investigation, and Laviron analysis consistently indicate the participation of approximately two electrons and one proton in the overall irreversible oxidation process. In addition, the cyclic voltammetric responses of SDN were compared with those of ciprofloxacin and ofloxacin (Figure 7), which are also nitrogen-containing heterocyclic pharmaceuticals. Ciprofloxacin and ofloxacin exhibited relatively sharp and well-defined oxidation peaks, whereas SDN showed a broader anodic response with less-defined peak characteristics. These observations suggest that the electrooxidation of SDN at the (S,N)-rGO/GCE may involve multistep electron-transfer reactions and/or adsorbed intermediates rather than a simple proton-coupled electron-transfer process. Furthermore, the presence of tertiary nitrogen centers and a flexible heterocyclic framework in SDN may promote strong interaction with the π-conjugated conductive surface, thereby altering the apparent proton participation during oxidation and contributing to the lower E_p–pH slope observed experimentally. Based on the E_p–pH relationship and Laviron analysis, the electrooxidation of SDN is hypothesized to involve an apparent two-electron/one-proton (2e$^-$/1H$^+$) transfer process. However, this interpretation should be considered a plausible hypothesis rather than a definitive reaction mechanism, as the oxidation of SDN is known to involve complex multistep electron-transfer reactions. Moreover, adsorption of SDN and/or its

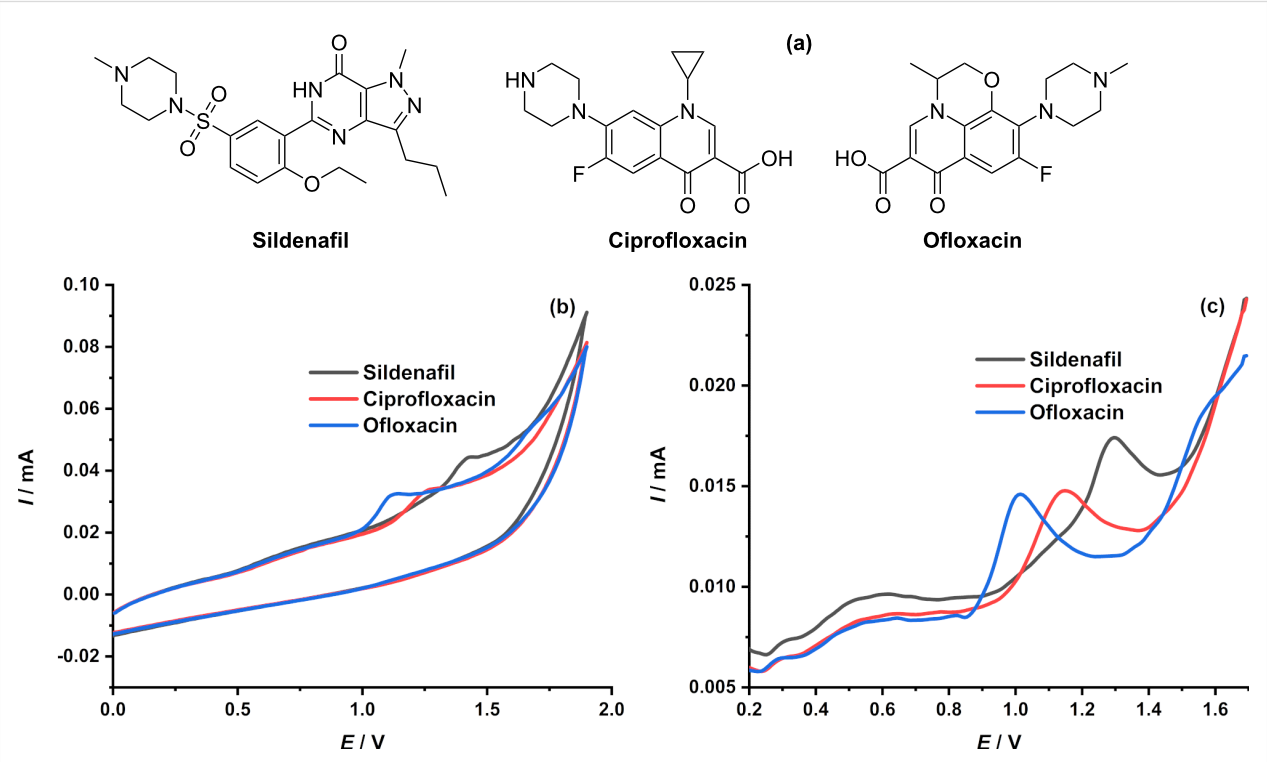

Figure 7: (a) Molecular structures, (b) CVs, and (c) DPVs of SDN, ciprofloxacin, and ofloxacin with concentration of 5.0 μM in 0.1 M BR buffer (pH 4.0).

oxidation intermediates on the (S,N)-rGO surface may influence the electrochemical response and the apparent kinetic parameters. Therefore, further mechanistic investigations, including in situ spectroelectrochemical measurements or identification of oxidation products, would be valuable for elucidating the detailed oxidation mechanism.

Optimizing operational parameters

The experimental parameters were optimized to achieve the best analytical performance (Supporting Information File 1, Figures S1–S4). The optimal conditions were determined as follows: accumulation potential of 0.4 V, accumulation time of 40 s, pulse amplitude of 0.10 V, and potential step of 0.007 V.

Linear range and limit of detection

The analytical performance of the proposed sensor was evaluated using DPV under the optimized conditions. As shown in Figure 8a, the oxidation peak current increases progressively with increasing SDN concentration from 0.25 to 19.61 µM. A good linear relationship between peak current and SDN concentration was obtained over this range (Figure 8b), described by the following equation:

$$I_{SDN} = (0.7945 \pm 0.0315) + (0.52501 \pm 0.0027) C_{SDN};$$
$$r^2 = 0.9993.$$

The LOD and the LOQ, calculated according to the criteria of 3S/b and 10S/b, respectively [34,35] were determined to be 0.49 and 1.61 µM. To further improve sensitivity at low concentrations, a narrower linear range (0.25–4.98 µM) was considered using eight concentration points near the origin. In this range, LOD and LOQ were significantly improved to 0.24 and 0.78 µM, respectively, demonstrating the enhanced detection capability of the sensor at trace levels.

As summarized in Table 2, the proposed (S,N)-rGO/GCE sensor exhibits a lower detection limit than most previously reported electrochemical sensors for SDN determination, while providing a wide linear range and satisfactory applicability for the analysis of pharmaceutical formulations.

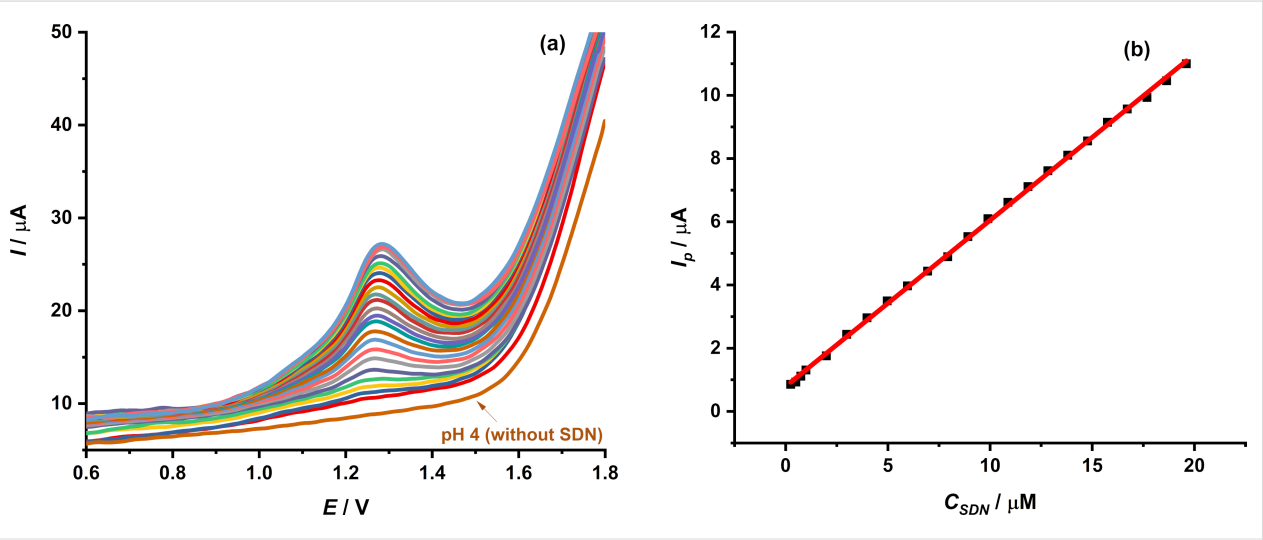

Figure 8: (a) DPV curves of (S,N)-rGO/GCE in 0.1 M Britton–Robinson buffer (pH 4.0) for different concentrations of C_{SDN} (0.25–19.61 µM); (b) corresponding calibration plot of peak current versus SDN concentration.

Table 2: Comparison of the analytical performance of electrochemical sensors for the determination of SDN.

Electrode	Method	Linear range (µM)	LOD (µM)	Application	Ref.
SPGCE	SWV	1.0–14.0	0.055	pharmaceutical and urine samples	[36]
SPCE	SWV	1.0–20.0	0.20	commercial and adulterated tablets	[37]
BDDE	DPV	0.730–7.3	0.64	pharmaceutical formulations	[38]
ABPUE-AgNP	DPV	1.0–10.0	0.89	pharmaceutical formulations and synthetic urine	[31]
Paraff-GE	SWV	25–250	9.0	pharmaceutical formulations	[39]
RuQT	DPV	12.5–500.0	10.7	pharmaceutical formulations	[40]
(S,N)-rGO/GCE	DPV	0.25–19.61	0.24	pharmaceutical formulations	this work

Repeatability, reproducibility, and long-term stability

Intra-day repeatability (within-electrode precision) of the proposed electrochemical method was evaluated at four representative concentration levels (1.0, 2.0, 13.8, and 19.6 µM) using replicate measurements (n = 3) (Figure 9a and Supporting Information File 1, Figure S5). At 1.0 µM, the peak current was 0.9585 ± 0.0469 µA, corresponding to an RSD of 4.90%, which is lower than the acceptable criterion of $0.5RSD_{Horwitz}$ = 8.50%. Similarly, at 2.0 µM, the peak current was 1.6990 ± 0.0732 µA with an RSD of 4.31%, also below the threshold ($0.5RSD_{Horwitz}$ = 7.66%). At higher concentrations, improved precision was observed, with RSD values of 1.30% and 1.02% for 13.8 and 19.6 µM, respectively, both significantly lower than the corresponding $0.5RSD_{Horwitz}$ values (5.73% and 5.43%) [41]. The electrode-to-electrode reproducibility of the sensor was further assessed using seven independently prepared electrodes at a fixed concentration of 13.8 µM (Figure 9b). The peak current was 7.9800 ± 0.1716 µA with an RSD of 2.15%, indicating good fabrication reproducibility. In addition, the long-term stability of the modified electrode was evaluated over seven consecutive days (Figure 9c). The average peak current was 7.8657 ± 0.1828 µA with an RSD of 2.32%, and the signal decreased by only 5.06% after seven days, demonstrating good storage stability. Overall, these results confirm that the proposed (S,N)-rGO/GCE sensor provides good precision, reproducibility, and stability, making it suitable for reliable electrochemical analysis.

Selectivity

The selectivity of the proposed electrochemical sensor was evaluated by investigating the effect of common inorganic ions and organic substances that may coexist with SDN (Supporting

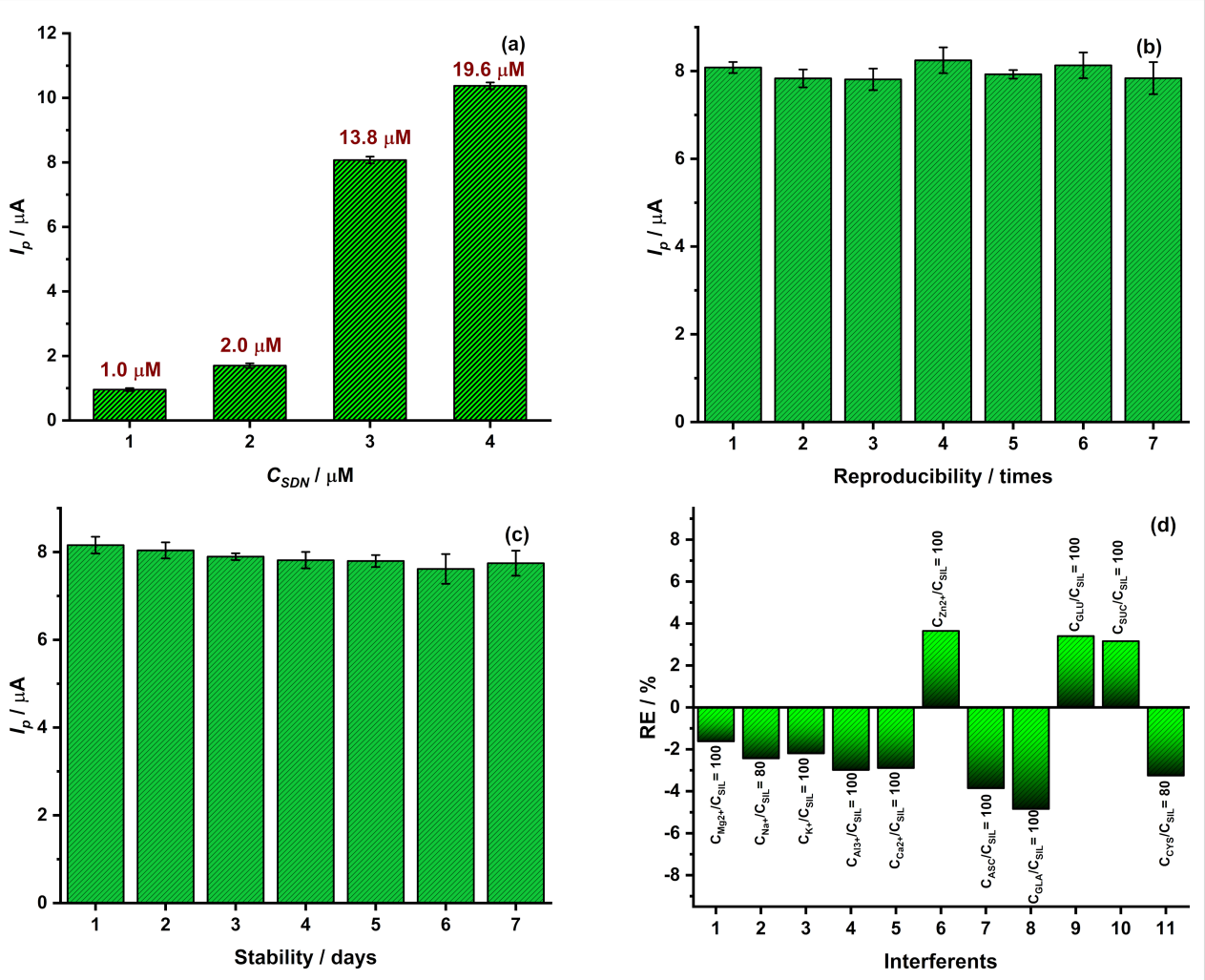

Figure 9: (a) Variation of peak current (I_p) for SDN at four concentrations (1.0, 2.0, 13.8, and 19.6 µM) recorded at the (S,N)-rGO/GCE in 0.1 M Britton–Robinson buffer (pH 4.0); (b) repeatability of the peak current at a fixed concentration (C_{SDN} = 13.8 µM) measured over seven successive determinations using the same electrode preparation procedure; (c) long-term stability of the sensor evaluated over seven consecutive days; (d) relative error (RE%) caused by interfering substances at different concentration ratios.

Information File 1, Table S1). Various potential interferents, including Mg^{2+}, Na^{+}, K^{+}, Al^{3+}, Zn^{2+}, and Ca^{2+}, as well as organic compounds such as ascorbic acid (ASC), glutamic acid (GLA), glucose (GLU), sucrose (SUC), and L-cysteine (CYS), were evaluated at concentration ratios ranging from 0 to 100-fold relative to SDN, except for Na^{+} and sucrose (SUC), which were investigated up to 80-fold (Figure 9d). As shown in Figure 9d, the presence of these interfering species caused only minor variations in the peak current of SDN. The relative error (RE) values were generally within ±5%, even at high interferent-to-analyte ratios (up to 100). In particular, most inorganic ions exhibited negligible interference, with RE values typically below ±3%. Organic compounds such as glucose and sucrose showed slight positive deviations, while ascorbic acid and L-cysteine resulted in small negative deviations, which can be attributed to their electroactive nature. However, these effects remained within acceptable analytical limits. According to commonly accepted criteria ($|RE| \leq 5\%$), these results demonstrate that the proposed (S,N)-rGO/GCE sensor possesses good selectivity for the determination of C_{SDN} in the presence of potential interfering substances. The high selectivity of the sensor suggests its strong potential for application in complex real samples.

Analysis of real sample

The applicability of the proposed (S,N)-rGO/GCE sensor was evaluated by determining SDN in commercial pharmaceutical samples using the DPV method. Three different products were analyzed, and the results are summarized in Table 3. The measured concentrations of C_{SDN} in the electrochemical cell were found to be 4.07 ± 0.07, 4.22 ± 0.08, and 4.05 ± 0.08 μM for samples 1–3, respectively. These values were converted to the corresponding SDN content per dosage unit, yielding 48.4, 102.5, and 47.6 mg, respectively. The analytical accuracy of the proposed sensor was evaluated using two complementary approaches. First, recovery experiments were carried out by the standard addition method, yielding satisfactory recoveries ranging from 97.6% to 103.5%. Second, the results obtained by the proposed DPV method were compared with those obtained using the reference HPLC method. No statistically significant difference was observed between the two methods, confirming the accuracy, reliability, and practical applicability of the developed electrochemical sensor for the determination of SDN in pharmaceutical formulations.

Although the developed (S,N)-rGO/GCE sensor demonstrated excellent analytical performance for the determination of SDN in pharmaceutical formulations, several limitations should be acknowledged. The present study focused exclusively on pharmaceutical samples, and therefore additional validation in more complex biological and environmental matrices is still required. Furthermore, while satisfactory stability was observed over a seven-day period, longer-term operational stability under routine analytical conditions remains to be investigated. The simple drop-casting fabrication procedure may also introduce slight variations in the modified film between independently prepared electrodes. In addition, although the sensor exhibited good selectivity toward the investigated interferents, structurally related electroactive compounds at relatively high concentrations could potentially influence the analytical response. Future work will focus on improving electrode fabrication reproducibility, extending the sensor lifetime, and evaluating its applicability in complex real-world samples.

Conclusion

In this study, an efficient electrochemical sensor based on a glassy carbon electrode modified with (S,N)-doped reduced graphene oxide ((S,N)-rGO) was successfully developed for the determination of SDN. The successful incorporation of nitrogen and sulfur into the graphene structure was confirmed by multiple characterization techniques, resulting in enhanced structural defects and improved electrochemical properties. The (S,N)-rGO/GCE exhibited excellent electrocatalytic activity toward SDN oxidation, enabling sensitive detection with a wide linear range (0.25–4.98 μM), a low limit of detection (0.24 μM), and a limit of quantification of 0.78 μM. The sensor also demonstrated good repeatability, reproducibility, and long-term stability, together with high selectivity in the presence of potential interfering species. Importantly, the proposed method was successfully applied to the analysis of pharmaceutical samples, and the results were in good agreement with those obtained by HPLC, confirming its accuracy and reliability. These

Table 3: Determination of SDN in commercial pharmaceutical samples using the proposed DPV method and comparison with the HPLC method.

Sample name	Found (μM)[a] ± SD (μM)	SDN (mg per unit, DPV)	SDN (mg per unit, HPLC)	Added (μM)	Found after spiking (μM) ± SD[a] (μM)	Recovery (%)
1	4.07 ± 0.07	48.4	51.5	1.00	5.06 ± 0.06	98.1
2	4.22 ± 0.08	102.5	102.0		5.36 ± 0.14	103.5
3	4.05 ± 0.08	47.6	48.7		5.06 ± 0.06	97.6

[a]Concentration calculated in the electrochemical cell.

findings indicate that the (S,N)-rGO-based electrochemical sensor provides a simple, cost-effective, and reliable alternative for the routine determination of SDN in real samples.

The proposed (S,N)-rGO-functionalized sensing platform offers several advantages, including a simple and low-cost fabrication process, enhanced electron-transfer capability, high electrocatalytic activity, satisfactory selectivity, and reliable determination of SDN in pharmaceutical formulations. Compared with conventional chromatographic techniques, the proposed electrochemical sensor provides rapid analysis with minimal sample preparation and lower instrumentation cost. Nevertheless, the current study is limited to pharmaceutical samples, and further investigations are required to evaluate long-term operational stability and its applicability to more complex biological and environmental matrices.

Supporting Information

Supporting Information File 1

Additional figures.
[https://www.beilstein-journals.org/bjnano/content/supplementary/2190-4286-17-74-S1.pdf]

Funding

Hue University partially funded this research under the Core Research Program No. NCTB.DHH.2025.05.

Author Contributions

Nguyen Quang Man: conceptualization; funding acquisition; writing – original draft. Ngo Thi Thanh Xuan: conceptualization; funding acquisition; writing – original draft. Vo Thi Khanh Ly: investigation; methodology; resources; validation; visualization. Le Van Thanh Son: investigation; methodology; resources; validation; visualization. Le Duc Anh: investigation; methodology; resources; validation; visualization. Le Thi Hong Phong: investigation; methodology; resources; validation; visualization. Nguyen Hai Phong: supervision. Pham Khac Lieu: investigation; methodology; resources; validation; visualization. Le Lam Son: investigation; methodology; resources; validation; visualization. Dinh Quang Khieu: writing – review & editing.

ORCID® iDs

Nguyen Quang Man - https://orcid.org/0000-0001-6511-1236
Ngo Thi Thanh Xuan - https://orcid.org/0009-0000-9270-5056
Vo Thi Khanh Ly - https://orcid.org/0009-0005-0854-3290
Le Van Thanh Son - https://orcid.org/0000-0002-2061-6983
Le Duc Anh - https://orcid.org/0000-0002-5940-8591
Le Thi Hong Phong - https://orcid.org/0000-0001-8825-6243
Nguyen Hai Phong - https://orcid.org/0000-0001-5354-1052
Pham Khac Lieu - https://orcid.org/0000-0002-9002-1416
Le Lam Son - https://orcid.org/0000-0002-8693-7472
Dinh Quang Khieu - https://orcid.org/0000-0003-3473-6377

Data Availability Statement

All data that supports the findings of this study is available in the published article and/or the supporting information of this article.

References

1. Ghantous, I.; Tlais, M.; El Khatib, A.; Ghantous, G.; Maroun, G.; Challita, A.; Ayek, M.; Barmo, G.; Sahyoun, M.; Kary, G. *Glob. Cardiol. Sci. Pract.* **2025,** *2025,* e202531. doi:10.21542/gcsp.2025.31
2. Maliyakal, J.; Vadnere, N.; Bherje, S.; Patel, M. *Trends Environ. Anal. Chem.* **2025,** *47,* e00273. doi:10.1016/j.teac.2025.e00273
3. Tian, X.-y.; Zhang, M.-m.; Sun, F.-r. *J. Chromatogr. A* **2026,** *1766,* 466581. doi:10.1016/j.chroma.2025.466581
4. Ahmed, A.; Abdellah, N.; Shaltout, E. *Mansoura J. Forensic Med. Clin. Toxicol.* **2019,** *27,* 43–56. doi:10.21608/mjfmct.2019.52475
5. Oltulu, Ç.; Çelik, S.; Daşman, M. *Istanbul J. Pharm.* **2023,** *53,* 219–228. doi:10.26650/istanbuljpharm.2023.1206425
6. Momtaz, M. A.; El-Desoky, H. S.; Rehab, A.; Belal, F. *Talanta Open* **2025,** *12,* 100540. doi:10.1016/j.talo.2025.100540
7. Al Dhakhri, H. H.; Alqassabi, F.; Alrasbi, I.; Alhinai, D.; Al Salty, S.; Pannu, S.; Al Balushi, S.; Khan, S. A.; Akhtar, M. J. *Int. J. Second. Metab.* **2025,** *12,* 297–305. doi:10.21448/ijsm.1518387
8. Zhang, Y.; Zhang, H.; Jia, Z.; Li, C.; Chen, L.; Jin, S. *ACS Appl. Nano Mater.* **2026,** *9,* 5576–5585. doi:10.1021/acsanm.6c00595
9. Minh, D. T. C.; Nhu, N. T. Q.; Thi, L. A.; Vu, L. V.; Lan, D. T. N.; Anh, N. T. K.; Ha, P. T. T. *J. Pharm. Biomed. Anal.* **2024,** *251,* 116392. doi:10.1016/j.jpba.2024.116392
10. Wei, T.; Zhang, Y.; Huang, J.; Yang, J.; Tian, Y.; Shen, Y. *Food Biosci.* **2024,** *59,* 103905. doi:10.1016/j.fbio.2024.103905
11. Li, G.; Pan, Q.; Zhang, C.; Wang, J.; Peng, C.; Wang, Z. *Anal. Chim. Acta* **2023,** *1280,* 341883. doi:10.1016/j.aca.2023.341883
12. Zeng, R.; Qiu, M.; Wan, Q.; Huang, Z.; Liu, X.; Tang, D.; Knopp, D. *Anal. Chem. (Washington, DC, U. S.)* **2022,** *94,* 15155–15161. doi:10.1021/acs.analchem.2c03606
13. Chen, S.; Tian, S.; Wang, Y.; Li, M.; Tang, D. *Biosens. Bioelectron.* **2025,** *278,* 117340. doi:10.1016/j.bios.2025.117340
14. Barzani, H. A. H.; Anwar Omer, R.; Salih Barzani, K. I.; Jawhar, Z. H.; Sulaiman, S. H. *Crit. Rev. Anal. Chem.* **2026,** 1–35. doi:10.1080/10408347.2025.2611097
15. Alarcon, R. T.; da Silva, R.; Bannach, G.; Cavalheiro, É. T. G. *ACS Omega* **2026,** *11,* 15452–15461. doi:10.1021/acsomega.5c13297
16. Mombeshora, E. T.; Muchuweni, E. *RSC Adv.* **2023,** *13,* 17633–17655. doi:10.1039/d3ra02098c
17. Boroujerdi, R.; Paul, R. *Nanomaterials* **2022,** *12,* 2250. doi:10.3390/nano12132250
18. Gong, H.; Hu, X.; Zeng, R.; Li, Y.; Xu, J.; Li, M.; Tang, D. *Sens. Actuators, B* **2022,** *369,* 132307. doi:10.1016/j.snb.2022.132307
19. Zhou, Q.; Lin, Y.; Zhang, K.; Li, M.; Tang, D. *Biosens. Bioelectron.* **2018,** *101,* 146–152. doi:10.1016/j.bios.2017.10.027

20. Turunc, E.; Ucar, A.; Binzet, R.; Martinez, F. *Microchem. J.* **2026,** *220,* 116697. doi:10.1016/j.microc.2025.116697
21. Periyasamy, G.; Annamalai, K.; Patil, I. M.; Kakade, B. *Diamond Relat. Mater.* **2021,** *114,* 108338. doi:10.1016/j.diamond.2021.108338
22. Ngô, T. T. X.; Lê, Đ. A.; Nguyn, Q. M. *Hue Univ. J. Sci. Nat. Sci.* **2025,** *134,* 91–100. doi:10.26459/hueunijns.v134i1c.7820
23. Marcano, D. C.; Kosynkin, D. V.; Berlin, J. M.; Sinitskii, A.; Sun, Z.; Slesarev, A.; Alemany, L. B.; Lu, W.; Tour, J. M. *ACS Nano* **2010,** *4,* 4806–4814. doi:10.1021/nn1006368
24. Amir Faiz, M. S.; Che Azurahanim, C. A.; Raba'ah, S. A.; Ruzniza, M. Z. *Results Phys.* **2020,** *16,* 102954. doi:10.1016/j.rinp.2020.102954
25. Rochman, R. A.; Wahyuningsih, S.; Ramelan, A. H.; Hanif, Q. A. Preparation of Nitrogen and Sulphur Co-Doped Reduced Graphene Oxide (RGO-NS) Using N and S Heteroatom of Thiourea. In *IOP Conference Series: Materials Science and Engineering, Vol. 509,* 2019. doi:10.1088/1757-899x/509/1/012119
26. Chang, Y.-S.; Chen, F.-K.; Tsai, D.-C.; Kuo, B.-H.; Shieu, F.-S. *Sci. Rep.* **2021,** *11,* 20719. doi:10.1038/s41598-021-99883-9
27. Bharath, G.; Anwer, S.; Mangalaraja, R. V.; Alhseinat, E.; Banat, F.; Ponpandian, N. *Sci. Rep.* **2018,** *8,* 5718. doi:10.1038/s41598-018-24066-y
28. Madbouly, L. A.; Mrkwitschka, P.; Stockmann, J. M.; Jones, E.; Radnik, J.; Hodoroaba, V.-D. *Surf. Interface Anal.* **2025,** *57,* 300–306. doi:10.1002/sia.7386
29. Tessier, F. *Materials* **2018,** *11,* 1331. doi:10.3390/ma11081331
30. Nguyen, V. T.; Manh, T. D.; Duyen, V. T.; Binh, N. T. M.; Van Duong, D.; Tu, N. T. T.; Toan, T. T. T.; Nhiem, D. N.; Son, L. L.; Nhan, D. Q.; Quyen, N. D. V.; Hoa, D. T. N.; Khieu, D. Q. *J. Nanopart. Res.* **2022,** *24,* 145. doi:10.1007/s11051-022-05522-3
31. da Silva, R.; Alarcon, R. T.; Cavalheiro, É. T. G. *J. Electroanal. Chem.* **2025,** *979,* 118938. doi:10.1016/j.jelechem.2025.118938
32. Laviron, E. *J. Electroanal. Chem. Interfacial Electrochem.* **1979,** *101,* 19–28. doi:10.1016/s0022-0728(79)80075-3
33. Li, C. *Colloids Surf., B* **2007,** *55,* 77–83. doi:10.1016/j.colsurfb.2006.11.009
34. Yu, Z.; Qiu, C.; Huang, L.; Gao, Y.; Tang, D. *Anal. Chem. (Washington, DC, U. S.)* **2023,** *95,* 4212–4219. doi:10.1021/acs.analchem.2c05617
35. Lin, Y.; Zhou, Q.; Tang, D.; Niessner, R.; Knopp, D. *Anal. Chem. (Washington, DC, U. S.)* **2017,** *89,* 5637–5645. doi:10.1021/acs.analchem.7b00942
36. Farghali, R. A.; Ahmed, R. A. *Int. J. Electrochem. Sci.* **2012,** *7,* 13008–13019. doi:10.1016/s1452-3981(23)16605-3
37. Rocha, D. S.; Silva-Neto, H. A.; de Oliveira, L. C.; Souza, S. G. G.; Santana, M. H. P.; Coltro, W. K. T. *Braz. J. Anal. Chem.* **2022,** *9,* 210–228. doi:10.30744/brjac.2179-3425.ar-65-2021
38. Batista, É. F.; Sartori, E. R.; Medeiros, R. A.; Rocha-Filho, R. C.; Fatibello-Filho, O. *Anal. Lett.* **2010,** *43,* 1046–1054. doi:10.1080/00032710903491153
39. Mendonça, R. X.; Buzzetti, P. H. M.; Silva, A. L.; Araújo, A. S.; Ponzio, E. A.; Semaan, F. S. *Rev. Virtual Quim.* **2015,** *7,* 1692–1708. doi:10.5935/1984-6835.20150096
40. Delolo, F. G.; Rodrigues, C.; da Silva, M. M.; Dinelli, L. R.; Delling, F. N.; Zukerman-Schpector, J.; Batista, A. A. *J. Braz. Chem. Soc.* **2014,** *25,* 550–559. doi:10.5935/0103-5053.20140031
41. Horwitz, W.; Albert, R. *J. AOAC Int.* **2006,** *89,* 1095–1109. doi:10.1093/jaoac/89.4.1095

License and Terms

BEILSTEIN JOURNAL OF NANOTECHNOLOGY

Synthesis of carbon dot-mediated gold nanostructures: experimental and quantum chemical insights into turn-on fluorescence sensing of *N*-acetylcysteine

Thuy-Huong Nguyen[1], Van-Nghia Nguyen[1], Ha Thi Thu Nguyen[1], Ha Ngoc Nguyen[2], Anh Duc Nguyen[3], Tuyen Viet Nguyen[4] and Truong Xuan Nguyen[*1]

Full Research Paper

Open Access

Address:
[1]School of Chemistry and Life Sciences, Hanoi University of Science and Technology, 01 Dai Co Viet, Hanoi, Vietnam, [2]Faculty of Chemistry, Hanoi National University of Education, 136 Xuan Thuy, Hanoi, Vietnam, [3]University of Science and Technology of Hanoi, Vietnam Academy of Science and Technology, 18 Hoang Quoc Viet, Hanoi, Vietnam and [4]University of Science, Vietnam National University, 334 Nguyen Trai, Hanoi, Vietnam

Email:
Thuy-Huong Nguyen - huong.NT221799@sis.hust.edu.vn;
Van-Nghia Nguyen - nghia.nguyenvan@hust.edu.vn;
Ha Thi Thu Nguyen - ha.nguyenthithu3@hust.edu.vn;
Ha Ngoc Nguyen - hann@hnue.edu.vn;
Anh Duc Nguyen - nguyen-duc.anh@usth.edu.vn;
Tuyen Viet Nguyen - nguyenviettuyen@hus.edu.vn;
Truong Xuan Nguyen[*] - truong.nguyenxuan@hust.edu.vn

* Corresponding author

Keywords:
fluorescence; gold nanoparticles; green synthesis; *N*-acetylcysteine; nitrogen-doped carbon dots

Beilstein J. Nanotechnol. **2026,** *17,* 1103–1116.
https://doi.org/10.3762/bjnano.17.75

Received: 09 May 2026
Accepted: 28 July 2026
Published: 12 August 2026

This article is part of the thematic issue "Innovative nanomaterials for next-generation bio- and chemosensing".

Guest Editor: Q. T. Duong

Abstract

In this work, a green and sustainable hydrothermal approach was employed to synthesize nitrogen-doped carbon dots (NCDs) using lemon juice as a natural precursor. The as-prepared NCDs served as eco-friendly reducing agents and stabilizing scaffolds for the subsequent in situ synthesis of gold nanoparticles (Au@NCDs). The structural and optical properties of the nanocomposite were comprehensively characterized using various analytical techniques. The intrinsic fluorescence of NCDs was significantly quenched upon formation of the composite, mainly due to non-radiative energy transfer processes. Interestingly, the quenched fluorescence could be efficiently restored upon the addition of *N*-acetylcysteine (NAC), enabling the development of an “off-on” fluorescent sensing platform. The sensing mechanism was systematically elucidated through a combination of spectroscopic studies and density functional theory calculations, revealing that fluorescence recovery originates from a ligand exchange process driven by the stronger binding affinity of NAC toward the gold surface, particularly via Au–S interactions. Under optimized conditions, the assay exhibited a robust linear response for NAC concentrations ranging from 4.0 to 20.0 mg/L, with a detection limit of 0.863 mg/L. These results demonstrate that the Au@NCDs system can function as a sensitive and selective OFF–ON fluorescent probe for NAC

detection. This study provides a cost-effective and eco-friendly sensing platform with significant potential for analytical applications in pharmaceutical monitoring.

Introduction

N-acetylcysteine (NAC) has been widely employed for over four decades as an antidote in the treatment of paracetamol (acetaminophen) overdose [1-3] and as a mucolytic agent for chronic obstructive pulmonary disease (COPD) [4]. Careful dosage control of NAC is crucial to ensure effective treatment and prevent side effects. Several analytical methods have been conventionally used to determine NAC levels in biological or pharmaceutical samples, including chromatography [5,6] and spectroscopy [7-9]. Currently, electrochemical and optical sensors are gaining prominence in clinical analysis due to their simplicity, requirement for small sample volumes, cost-effectiveness, high specificity, and selectivity [10-16].

Carbon quantum dots (CQDs or CDs) have garnered significant attention due to their strong fluorescence and exhibit significant potential in applications such as photocatalysis, bioimaging, bioanalytical sensing, and pharmaceutical testing [17]. CDs can be synthesized from diverse precursors, including citric acid, carbohydrates, and organic molecules through two distinct methodologies, that are, bottom-up and top-down methods [18,19]. In recent years, carbon dots derived from natural sources have increasingly attracted interest as a sustainable and environmentally friendly approach [20-22]. Natural precursor sources, including plant extracts, fruits, and vegetables (e.g., orange juice [23], turmeric [24], lemon juice [25], mango leaves [26], and guava leaves [27]), are abundant, inexpensive, and renewable carbon sources. Furthermore, they contain various organic compounds with hydroxy, carboxyl, and amino groups. Consequently, natural-product-derived carbon dots frequently demonstrate high hydrophilicity, excellent biocompatibility, and a broader spectrum of surface functional groups compared with CDs synthesised from chemical precursors [28-30].

Among the various strategies aimed at improving the physicochemical properties of CDs, heteroatomic doping has been extensively studied [31]. Nitrogen-doped carbon dots (NCDs) are formed by introducing nitrogen atoms into carbon frameworks or functional groups on the surface. Nitrogen doping alters the electronic structure of the carbon core and creates surface functional groups such as amine and pyridinic groups. Compared with undoped carbon dots, NCDs featured excellent robust fluorescence stability and chemical resistance [32].

Fluorescent probes are powerful analytical tools favored for their rapid response, high sensitivity, simplicity, low cost, and real-time detection capabilities. To overcome the inherent limitations of organic dyes, nanomaterial-based sensing platforms have attracted considerable research interest. In particular, gold-based composite nanoparticles stand out as promising candidates for advanced fluorescent probes, owing to their exceptional optical properties, large specific surface area, excellent biocompatibility, and ease of surface functionalization [33]. A key feature of gold nanoparticles is their surface plasmon resonance, which generates strong light–matter interactions, amplifies optical signals, and underpins their extensive application in optical sensing [34].

This study developed an OFF–ON fluorescent sensor based on gold nanoparticles and nitrogen-doped carbon dots (Au@NCDs) for the determination of NAC. NCDs, possessing strong luminescence properties, served as both reducing agent and stabilizing agent for the synthesis of Au@NCDs [35]. Upon excitation of the NCDs, the energy was transferred to the gold nanoparticles, resulting in fluorescent quenching. With the addition of NAC, a ligand exchange occurred between the thiol groups of NAC and the NCDs on the gold nanoparticles surface, resulting in the formation of a stronger Au–S bond and the subsequent recovery of the fluorescent signal. The restored fluorescence intensity exhibited a proportional relationship with the concentration of the added NAC.

In addition to experimental characterization, density functional theory (DFT) calculations have emerged as a powerful approach for elucidating the molecular-level mechanisms governing the performance of nanomaterial-based fluorescent sensors [36-38]. DFT provides valuable insights into adsorption configurations, binding energies, charge redistribution, and electronic structures, thereby enabling the interpretation of analyte–nanomaterial interactions that are often difficult to resolve experimentally. In particular, for gold nanostructure-based sensing platforms, DFT has been widely employed to investigate the formation and stability of Au–S bonds [39,40], ligand exchange processes [41,42], and the associated electronic changes responsible for fluorescence quenching and recovery [43-45]. Therefore, integrating DFT calculations with experimental studies offers a comprehensive understanding of the sensing mechanism and facilitates the rational design of highly sensitive fluorescent nanosensors.

Although carbon dots and gold nanoparticles have been widely investigated for fluorescence sensing, the development of lime

juice-synthesized carbon dot-mediated gold nanostructures with mechanistic insight into their fluorescence response toward NAC remains limited. In particular, the relationship between the structural and electronic properties of Au@NCD nanocomposites and their fluorescence sensing behavior has not been fully understood. Therefore, the novelty of this study lies not only in using a natural source for synthesis of Au@NCD nanostructures but also in the combination of experimental and theoretical approaches to provide mechanistic insights into the fluorescence sensing process.

Experimental

Chemicals and instrumentation

Tetrachloroauric(III) acid trihydrate (99.5%), urea (99.5%), dimethylformamide (DMF, ≥99.8%), acetone (≥99.8%), and silicagel 60 (0.015–0.040 mm) were purchased from Merck, USA. *N*-Acetylcysteine ≥98% and ethanol 95% were supplied by ThermoFisher, USA. Acetonitrile (ACN, ≥99.9%) was bought from Fisher Scientific, England. Fresh lime juice was prepared from limes (*Citrus* × *aurantiifolia*) obtained from a local supermarket in Hanoi, Vietnam. The chemicals were used as received, and their solutions were prepared in double distilled water. Fluorescence measurements were carried out using a Jasco FP-6500 spectrofluorometer (Japan). Absorption spectra were collected on an Agilent 8453 UV–vis spectrophotometer (USA). Fourier-transform infrared (FTIR) spectra were recorded by a Nicolet iS50 spectrometer from Thermo Scientific (Japan). Morphologies and sizes of the products were characterized using a JEOL JEM-1010 Transmission electron microscope (TEM), and a JEOL JSM-IT800 field emission scanning electron microscope (FESEM) (Japan). The elemental analysis was carried out on an Oxford EDX Ultim Max 65 (England) coupled with the FESEM instrument. Raman spectra of the samples were taken with an acquisition time of 60 s in two cycles by using HR 800 spectrometer from Horiba Jobin Yvon (France). The size distribution was characterized using a dynamic light scattering (DLS) Instrument (Horiba SZ-100-Z2, Japan). The glass chromatographic column with 45 cm in length and 2 cm in diameter was purchased from Duran, Germany.

Synthesis of nitrogen-doped carbon dots

NCDs were synthesized via a modified hydrothermal method [46]. Typically, a mixture of 20 mL of fresh lemon juice and 0.8 g of urea was stirred, transferred into a 50 mL Teflon-lined autoclave, and heated at 180 °C for 3 h. Afterward, the autoclave was allowed to cool naturally to room temperature. The resulting mixture was purified by gradient silica gel column chromatography, using approximately 100 mL acetone followed by 250 mL acetone/distilled water mixture (4:1, v/v) as the mobile phase. The purified CD fractions were identified by collecting sequential eluates and monitoring their fluorescence under UV light (365 nm) and PL spectroscopy. Fractions exhibiting an intense characteristic fluorescence of CDs were combined, while non-fluorescent or weakly fluorescent fractions were discarded [47].

Preparation of Au@NCDs composite

The synthesis conditions of Au@NCDs composites were primarily optimized including NCDs/$HAuCl_4$ ratio, temperature, and reaction time (see section 2 in Supporting Information File 1). The Au@NCDs composite was obtained by adding 2.5 mL of a NCD solution (0.15 mg/mL) to 2.5 mL of 0.2 mM $HAuCl_4$ under continuous stirring and heating at 60 °C. After 5 min, the solution gradually changed in color from yellow to pink. The mixture was then left at room temperature for 15 min before use [16,48]. The resulting mixture was centrifuged at 10,000 rpm for 30 min, and the supernatant was discarded. The precipitate was redispersed in deionized water (DW) and stored for further use.

Optimization of the organic solvent composition

The effect of the organic solvent on the fluorescence response of the Au@NCDs sensing system was investigated using mixtures of aqueous and organic solvents. Methanol, ethanol, acetone, ACN, and DMF were individually mixed with DW at a volume ratio of 25:75 (v/v). NAC standard solutions (25 mg/L) were prepared in each solvent mixture under identical conditions.

For each experiment, an aliquot of the Au@NCDs probe was mixed with the corresponding NAC solution, and the fluorescence intensity was recorded after incubation under the optimized sensing conditions described in section “Preparation of Au@NCDs composite”. The fluorescence recovery was evaluated as the change in fluorescence intensity (ΔI), calculated from the difference between the fluorescence intensity of the Au@NCDs probe in the presence (I) and absence (I_0) of NAC ($\Delta I = I - I_0$). All measurements were performed in triplicate, and the average values were used for comparison.

After identifying DMF as the most suitable organic solvent, its proportion in the water/DMF mixture was further optimized. Water/DMF mixtures containing 5%, 10%, 15%, 20%, and 25% (v/v) DMF were prepared while maintaining the NAC concentration at 25 mg/L. Fluorescence measurements were carried out under identical experimental conditions, and the corresponding fluorescence recovery (ΔI) was compared to determine the optimal solvent composition. Based on these experiments, a water/DMF mixture containing 25% (v/v) DMF was selected and used for all subsequent fluorescence sensing experiments.

Assay of *N*-acetylcysteine

Fresh standard NAC solutions were prepared prior to analysis and only stable Au@NCDs dispersions prepared using the same synthesis protocol were used for measurements. A mixture of DW and DMF solvent was used as a blank to zero background signals. All fluorescence measurements were performed under identical instrumental conditions and each experiment was conducted in triplicate. A specific amount of DMF solvent was added to 1 mL of Au@CDs solution, followed by 0.5 mL of NAC standard solution at concentration ranging from 1.0 to 80.0 mg/L. The resulting mixture was then equilibrated for 5 min. Subsequently, the fluorescent spectra of the prepared solutions were recorded. All measurements were performed in triplicate, and the average values were used for calculation. The analytical linear range and limit of detection were calculated from the obtained data.

Computational details

All calculations were carried out within the framework of DFT using the SIESTA package [49]. The exchange–correlation energy was described by the generalized gradient approximation with the Perdew–Burke–Ernzerhof functional [50]. Dispersion interactions were included using the Grimme DFT-D3 dispersion correction scheme with default parameters [51,52]. Norm-conserving pseudopotentials were used to represent the ionic cores, and valence states were expanded in a double-ζ plus polarization (DZP) numerical atomic orbital basis set for all atoms. The real-space integration grid was defined by a mesh cutoff of 4761.99 eV, which was verified to ensure convergence of total energies. Electronic occupations were treated using a Fermi–Dirac distribution at 300 K. Self-consistent field calculations were performed using the diagonalization method with Pulay mixing (mixing weight 0.15). Spin-polarized calculations were employed throughout the study.

The simulated system consisted of a gold nanocluster containing 249 Au atoms, which serves as a representative model for metallic Au nanoparticles (Au NPs) [53], interacting with a NCD model and NAC (Figure 1). The optimized structure of NAC shows good agreement with experimental data, with calculated geometric parameters deviating from reported values by approximately 1.17–3.4% (see Figure S2 and Table S2 in Supporting Information File 1), confirming the reliability of the computational approach. The NCD structure was constructed based on reported structural models, incorporating surface functional groups such as $–NH_2$, –OH, and –COOH. The model consists of 54 atoms, with edge carbon atoms hydrogen-passivated to satisfy valence requirements. All systems were modeled under periodic boundary conditions using sufficiently large simulation cells to avoid interactions between periodic images. Owing to the presence of acidic functional groups (–COOH, –SH), the interactions between NAC/NCD and Au NPs were systematically investigated for both neutral species (NAC and NCD) and their corresponding deprotonated forms (NAC^- and NCD^-). This approach allowed for a comprehensive evaluation of binding behavior under different chemical environments and provides a basis for understanding the ligand exchange mechanism discussed in subsequent sections.

Results and Discussion

Structural and morphological analysis

Characteristic functional groups of NCDs such as hydroxy, amine, carboxyl and carbonyl groups [54-56] are evident in the FTIR spectrum in Figure 2. Specifically, the broad absorption band in the 3000 to 3500 cm^{-1} region can be attributed to the stretching vibration of –NH/–OH group ($\upsilon_{N–H}/\upsilon_{O–H}$). Absorption peaks around 1635 cm^{-1} (shoulder) and 1569 cm^{-1} are assigned to $\upsilon_{C=O}$, while peaks at 1390 cm^{-1} correspond to C–N

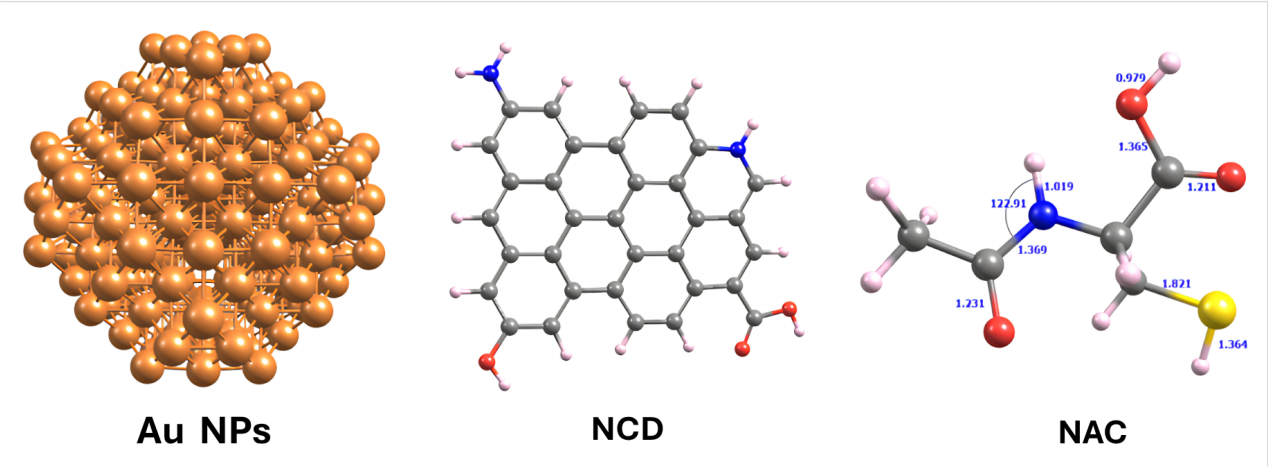

Figure 1: Optimized structures of (a) Au NPs, (b) NCD, (c) NAC. Color codes: light brown – Au, grey – C, blue – N, red – O, yellow – S, ivory – H. All key distances are in angstroms, angles are in degrees.

stretching vibrations. Vibration of –CO/CN/CH groups are responsible for the absorption peaks around 1078 cm^{-1}. The C–H stretching vibrations of benzene are represented by the peak at 786 cm^{-1}.

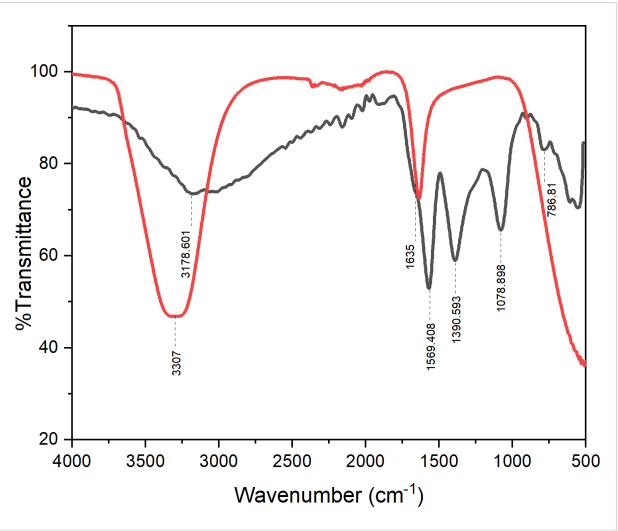

Figure 2: FTIR spectra of NCDs (black line) and Au@NCDs (red line).

Figure 3 shows the Raman spectra of NCDs and Au@NCDs. The NCD spectrum lacked discernible peaks due to significant fluorescence interference while Au@NCDs clearly shows the D band and the G band of carbon at 1360 and 1530 cm^{-1}, respectively [17]. Fluorescence quenching of carbon dots by Au nanostructures is a well-documented phenomenon where the fluorescence intensity of CDs decreases upon the addition of Au^{3+}. The quenching of the NCDs' photoluminescence can occur due to different mechanisms. The quenching can be attributed to a redox reaction where the Au^{3+} ions interact with the surface functional groups of the CDs, leading to a redox reaction, disrupting the normal radiative decay of the excited state in the CDs and thus reducing fluorescence [57]. Another mechanism for quenching is aggregation [58]. Reaction with Au^{3+} can also induce aggregation of the CDs, leading to a reduction of surface area and increased non-radiative decay pathways, while suppressing the fluorescence process. Moreover, the fluorescence of CDs might be quenched through fluorescence resonance energy transfer (FRET), a process involving energy transfer from the CD donor to the AuNP acceptor [59,60].

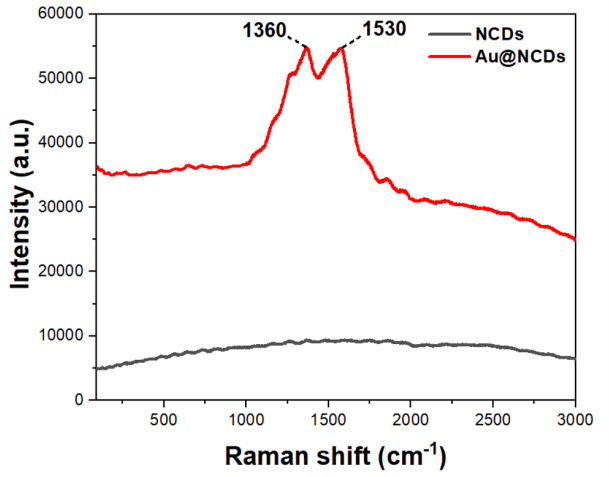

Figure 3: Raman spectra of NCDs and Au@NCDs.

As can be seen in Figure 4a, NCDs tend to form clusters with an average size of 30 nm size. In contrast, a mixture of spherical, polyhedral, triangular, and rod-like Au nanostructures is observed with Au@NCDs (Figure 4b). The diameter of Au NPs was approximately 35 nm, which is in agreement with dynamic laser scattering (DLS) analysis (Figure 4c). Indeed, the DLS results showed that the Au@NCD nanoparticles have sizes from 20 to 90 nm, while the average value is 35 ± 16.4 nm. The recorded PDI of 0.35 for the Au@NCDs indicated a highly polydispersed system resulting from a mixture of different structural Au nanoparticles. In addition, the zeta potential of

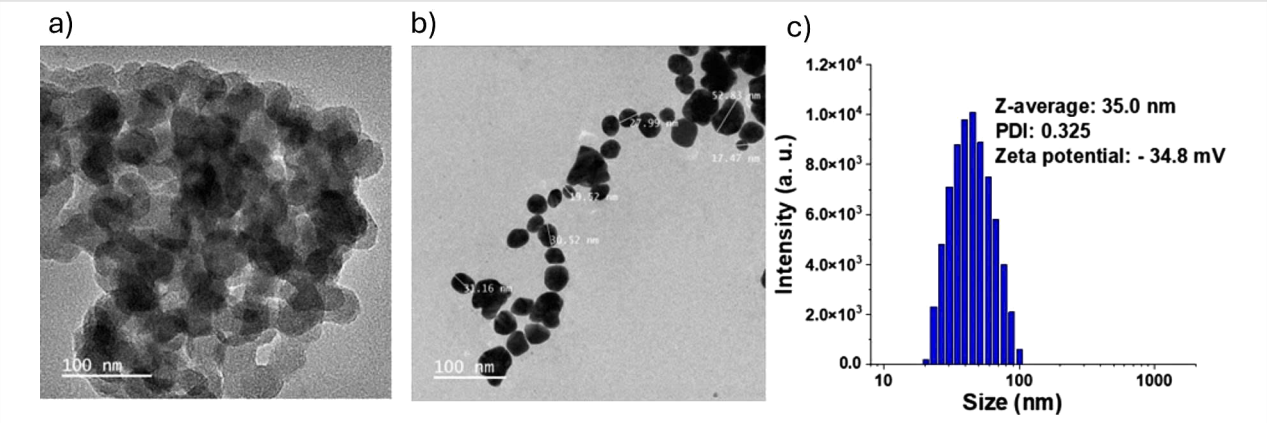

Figure 4: TEM images of (a) NCDs and (b) Au@NCDs and (c) DLS size distribution analysis of Au@NCDs.

−34.8 mV indicated a stable colloidal solution of Au@NCDs in water.

The element distribution on Au@NCDs and Au@NCDs-NAC were analyzed by FESEM in combination with energy dispersed X-ray spectroscopy as shown in Figure 5 and Figure 6, respectively. The spectra indicated that there were Au and C in Au@NCDs and Au, C, N, and S in Au@NCDs-NAC. The Au and C mapping images revealed the strong interaction between Au nanoparticles and NCDs in all samples. The presence of S in the EDX spectra of Au@NCDs-NAC suggested that the NAC molecules have interacted closely with NCDs.

Photophysical properties

Figure 7a shows the absorption spectra of NCDs and Au@NCDs. A distinct peak at 340 nm can be assigned to the π→π* transition of carbonyl C=O bonds present on the surface of NCDs. In the absorption spectrum of the Au@NCDs composite, this characteristic peak vanished due to the strong electronic interactions between the gold nanoparticles and NCDs [16]. Furthermore, the formation of Au NPs is confirmed by the presence of a broad surface plasmon resonance band centered around 550 nm.

Figure 7b presents photoluminescence (PL) spectra of NCDs and Au@NCDs when excited at 355 nm. It can be seen clearly that the Au nanoparticles quenched the fluorescence of NCDs, which is in agreement with the Raman data. Fluorescence quenching of NCDs can be attributed to several factors. The fluorescence of NCDs might be quenched through FRET. Such mechanism is reasonable as evidence by the spectral overlap of NCDs emission and Au@NCDs absorption.

Application of Au@NCDs as a fluorescent probe for detection of *N*-acetylcysteine

Sensing mechanism

The mechanism of NAC detection by the Au@NCDs probe is schematically illustrated in Figure 8a. In this system, NCDs act as light-harvesting antennae, efficiently absorbing incident photons and generating excited electronic states. The calculated

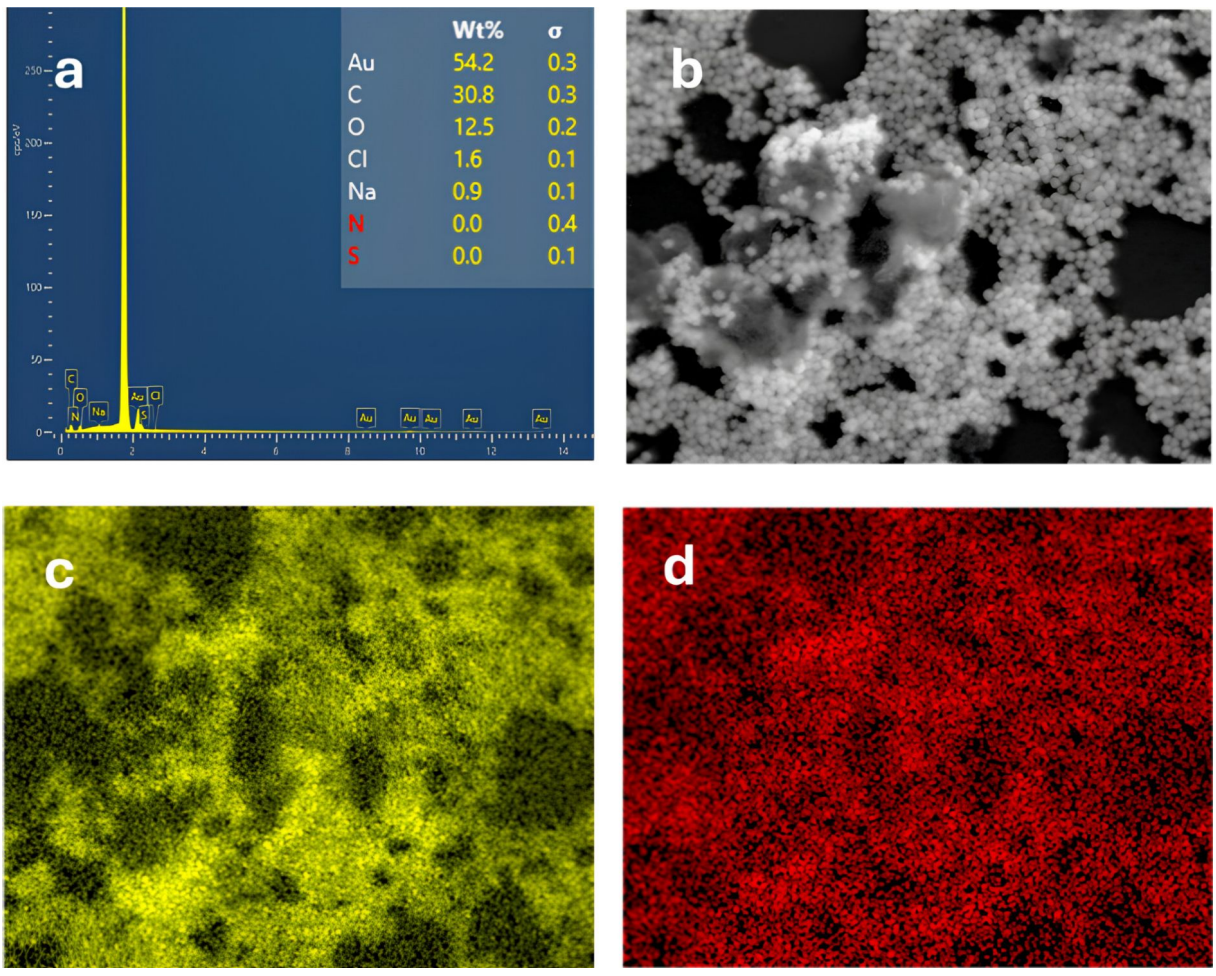

Figure 5: (a) EDX spectrum with elemental weight percentages, (b) SEM image, and elemental mapping of (c) Au and (d) C in Au@NCDs.

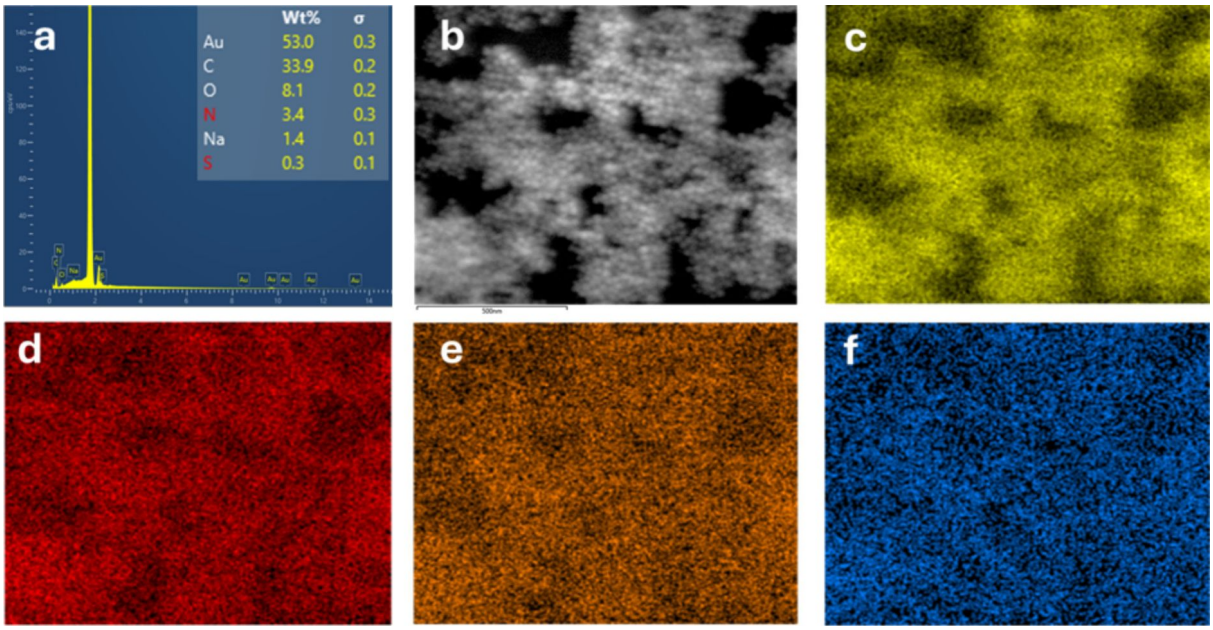

Figure 6: (a) EDX spectrum with elemental weight percentages, (b) SEM image, and elemental mapping of (c) Au, (d) C, (e) S, and (f) N in Au@NCDs-NAC.

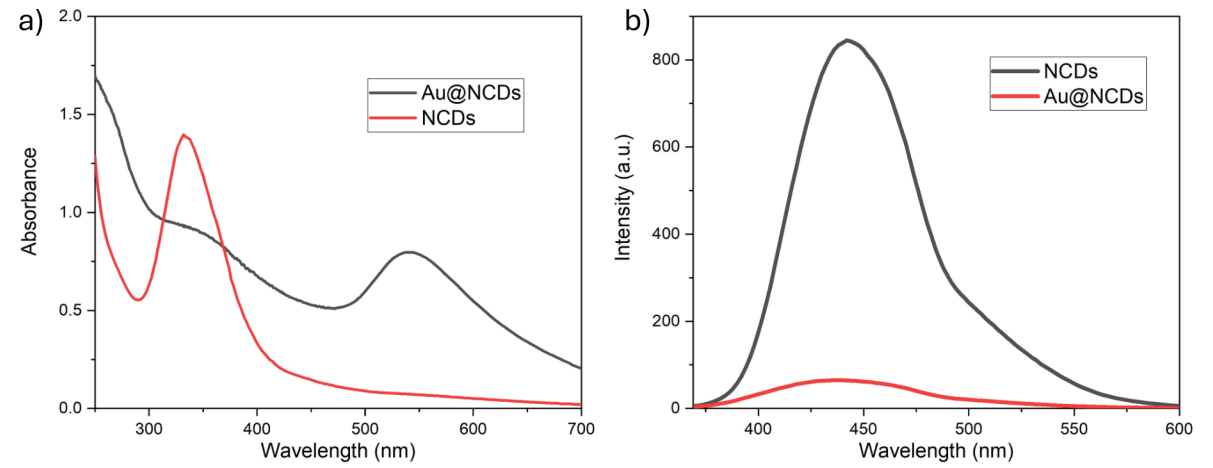

Figure 7: (a) Absorption and (b) photoluminescence spectra of NCDs and Au@NCDs (λ_{ex} = 355 nm).

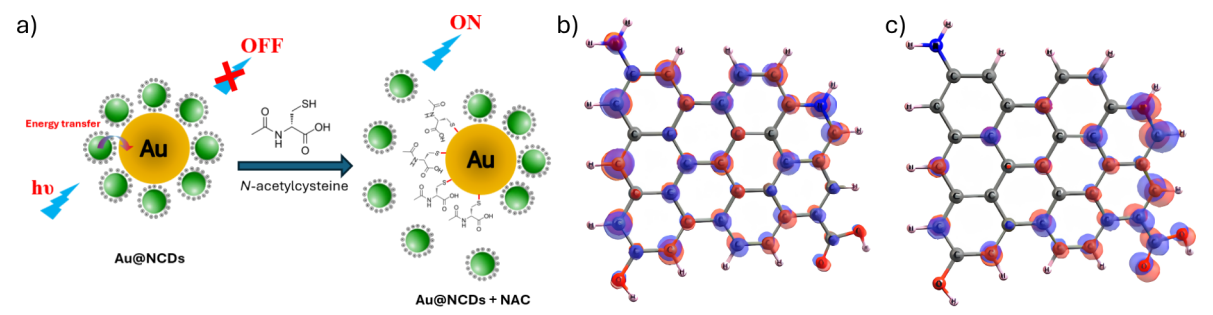

Figure 8: (a) Schematic illustration of the NAC detection mechanism of the Au@NCDs probe, (b, c) spatial distributions of the HOMO and LUMO of NCDs.

frontier orbital energies of NCDs show that the HOMO and LUMO are located at −8.5746 and −8.0600 eV, respectively, corresponding to a relatively small energy gap (≈0.51 eV), which facilitates photoexcitation under mild conditions.

The spatial distribution of the frontier orbitals further reveals that the HOMO is mainly localized on the π-conjugated carbon framework, while the LUMO is more delocalized and extends toward surface functional groups containing heteroatoms such as oxygen and nitrogen, consistent with previous reports on heteroatom-doped carbon dots (Figure 8b,c). This redistribution of electron density upon excitation suggests a partial intramolecular charge transfer character, enhancing the photoactive nature of NCDs and supporting their role as effective energy donors [61]. Rather than undergoing direct electron transfer, the excitation energy is transferred to Au nanoparticles via a non-radiative energy transfer process, likely mediated by plasmonic coupling or dipole–metal interactions. Notably, Au NPs exhibit a near-zero HOMO–LUMO gap, reflecting their metallic electronic structure and quasi-continuous density of states, which renders a discrete frontier orbital description inappropriate. Therefore, Au NPs function as efficient energy acceptors, where the transferred excitation energy is rapidly dissipated through non-radiative relaxation pathways, leading to fluorescence quenching (OFF state).

Upon the introduction of NAC, a ligand exchange process is proposed to occur, in which NAC molecules displace NCDs from the Au NPs surface. This behavior can be attributed to the stronger binding affinity of NAC toward Au. This proposed mechanism is further supported and rationalized by quantum chemical calculations. The computed interaction energies for Au NPs interacting with NCD and NAC provide molecular-level insight into their relative binding strengths, confirming the preferential adsorption of NAC on the Au NPs surface. These results offer a deeper understanding of the microscopic origin of the ligand exchange process and its role in modulating the fluorescence response of the Au@NCDs probe. The interaction energy E_{int} is defined as:

$$E_{int} = E(\text{Au NPs} + \text{substrate}) - E(\text{Au NPs}) - E(\text{substrate}),$$

where (E(Au NPs + substrate), E(Au NPs), E(substrate) denote the total energies of the Au NPs bound to the substrate (NCD, NAC, NCD^-, or NAC^-), the isolated Au NPs, and the isolated substrate molecules (NCD, NAC, NCD^-, or NAC^-), respectively.

First, the interaction between Au NPs and NCD was evaluated. Owing to the presence of several functional groups on its surface, Au NPs can interact with NCD at multiple sites, namely, via the –COOH group (forming AuNCD–COOH), via the $–NH_2$ group (forming AuNCD–NH_2), via the –OH group (forming AuNCD–OH), and through interaction with the deprotonated NCD^- species, assuming proton dissociation from the –COOH group to form AuNCD–COO^-. The optimized structures along with the corresponding E_{int} are presented in Figure 9.

Among the considered configurations, the deprotonated carboxyl group ($–COO^-$) exhibits the strongest interaction with the Au surface, with an E_{int} of −4.270 eV, which can be attributed to enhanced electrostatic attraction and strong Au–O coordination. The relatively short interaction distances (2.19–2.25 Å) further support the formation of stable binding in this configuration. In comparison, the neutral –COOH and $–NH_2$ groups show moderate interaction strengths, suggesting coordination interactions through lone pair donation from O or N atoms to the Au surface. The –OH group exhibits the weakest interaction (E_{int} = −1.467 eV). These results demonstrate that NCDs can bind to Au NPs through multiple functional groups with varying affinities, depending on their chemical state. Importantly, this moderate and tunable binding suggests that the NCD layer on Au NPs may be susceptible to displacement by ligands with stronger binding affinity, which will be further discussed in comparison with NAC.

Building upon the analysis of Au NPs and NCD interactions, it is essential to further examine the binding behavior of NAC on the Au surface in order to understand the ligand exchange mechanism. The optimized structures, together with their corresponding interaction energies (Figure 10), provide detailed insight into the binding characteristics of NAC on the Au NPs surface.

Among these configurations, the thiol group (–SH) plays a dominant role in anchoring NAC onto Au NPs. Even when the –COOH group is initially oriented toward the surface, structural optimization consistently leads to a configuration in which NAC binds through the thiol group, with an interaction energy of approximately −2.575 eV. This value is weaker than the configuration in which NAC simultaneously interacts with the Au surface via both the –SH and –COOH groups, which yields a stronger interaction energy of −3.306 eV. It is noted that, the deprotonated thiolate form ($–S^-$) exhibits significantly stronger binding, with an interaction energy of −6.378 eV, due to enhanced electron donation and stronger Au–S coordination, often accompanied by multipoint bonding interactions with the Au surface. These results clearly indicate that NAC interacts predominantly and most strongly with Au NPs through the sulfur head group. Importantly, when compared with the NCD system, NAC consistently exhibits more negative interaction energies,

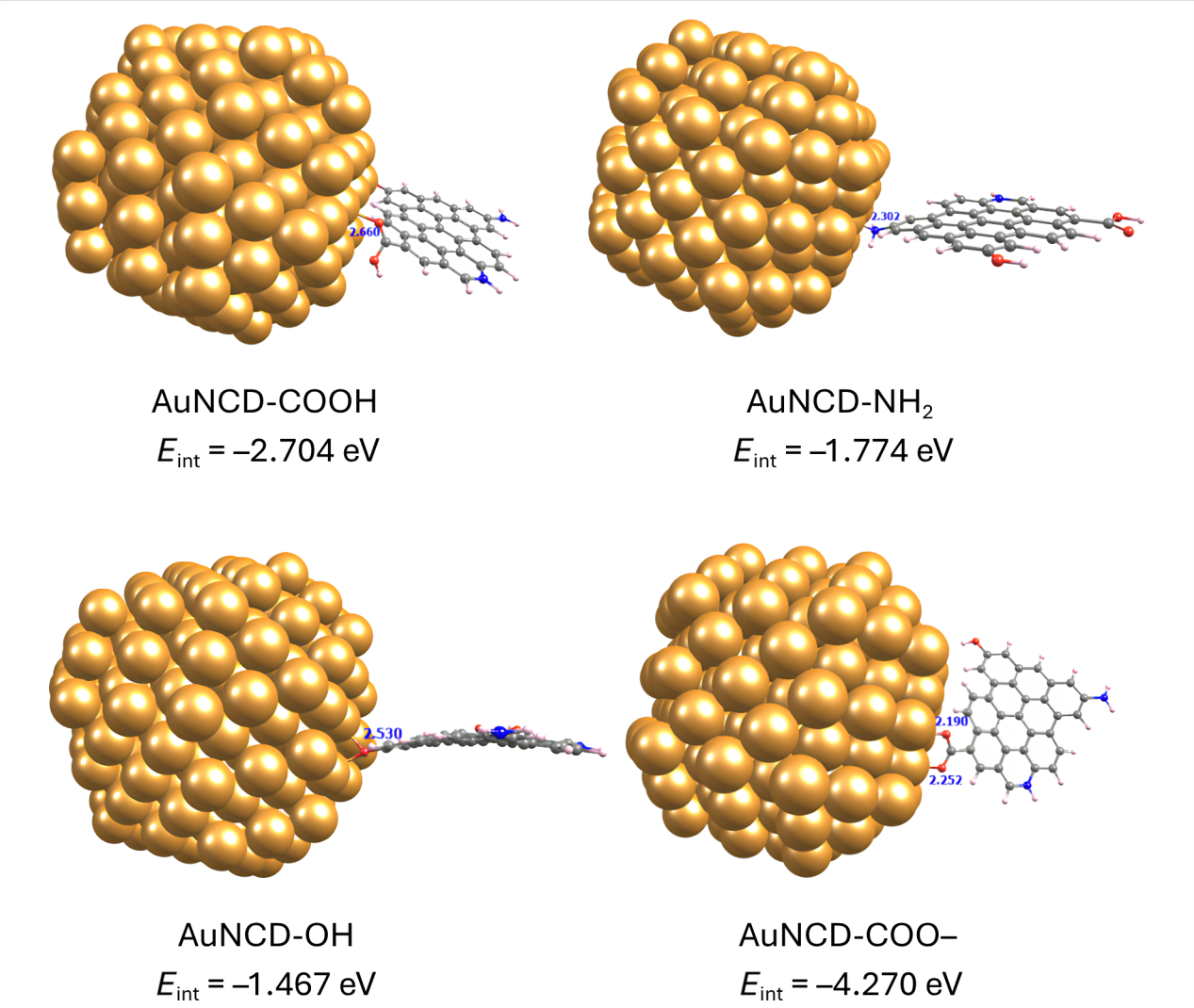

Figure 9: Optimized structures of the binding modes between Au NPs and NCD, along with the corresponding interaction energies.

indicating a stronger binding affinity toward Au NPs. This difference provides a thermodynamic driving force for the ligand exchange process, in which NAC molecules effectively displace NCDs from the Au surface. As a consequence, the displacement of NCDs disrupts the energy transfer pathway between NCDs and Au NPs, thereby restoring the fluorescence signal (ON state) of the sensing system. These results clearly indicate that NAC interacts predominantly and most strongly with Au NPs through the sulfur head group. Importantly, when compared with the NCD system, NAC consistently exhibits more negative interaction energies, indicating a stronger binding affinity toward Au NPs. This difference provides a thermodynamic driving force for the ligand exchange process, in which NAC molecules effectively displace NCDs from the Au surface. The stronger adsorption of NAC increases the separation between NCDs and Au nanoparticles, thereby disrupting the non-radiative energy transfer pathway responsible for fluorescence quenching. Because this energy transfer is highly dependent on the close proximity between NCDs and Au nanoparticles, weakening their interaction suppresses the quenching process and restores the fluorescence emission of NCDs, giving rise to the characteristic OFF–ON fluorescence response. This mechanistic interpretation establishes a direct correlation between the DFT-calculated interaction energies and the experimental photoluminescence results. The proposed ligand exchange mechanism and the associated fluorescence recovery are further supported by experimental evidence from PL spectra (Figure 11).

As shown, pristine NCDs exhibit strong fluorescence emission, whereas the emission intensity is significantly quenched upon formation of Au@NCDs, confirming the effective non-radiative energy transfer from NCDs to Au NPs (OFF state). Upon the introduction of NAC, the fluorescence intensity is partially

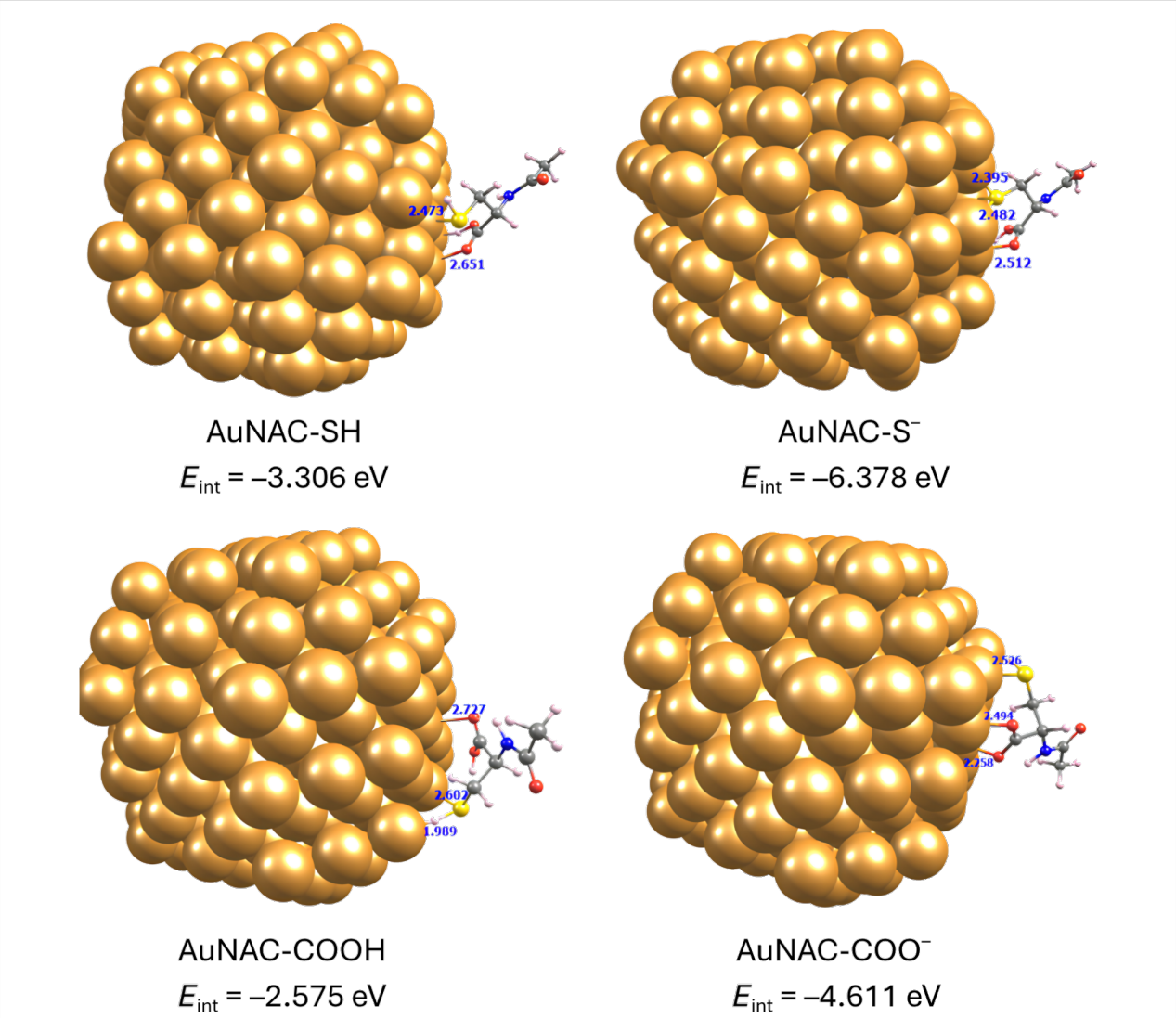

Figure 10: Optimized structures of the binding modes between Au NPs and NAC, along with the corresponding interaction energies.

restored, indicating disruption of the NCD–Au interaction and suppression of the energy transfer pathway. This recovery (ON state) is consistent with the displacement of NCDs from the Au surface by NAC molecules, as suggested by the stronger binding affinity of NAC revealed in the theoretical calculations. Furthermore, previous studies have reported that gold nanocomposites exhibit good selectivity toward NAC, suggesting that the proposed CD@Au nanocomposite is also likely to be selective for NAC [11].

Additional evidence supporting the proposed sensing mechanism can be obtained from Raman spectroscopy (Figure S3 in Supporting Information File 1). In the presence of NAC, the Raman intensity corresponding to the C–H bending (δ_{CH}) vibrations decreases, which can be attributed to the recovery of NCD fluorescence. This behavior is consistent with the fluorescence–Raman interplay, where enhanced fluorescence emission can partially suppress Raman signals. Taken together, both the PL and Raman results are in good agreement with the theoretical findings, providing complementary evidence for the ligand exchange-driven sensing mechanism and the associated OFF–ON fluorescence response of the Au@NCDs probe.

Effect of organic solvent

Figure 12a illustrates the fluorescence response of the Au@NCDs probe in a 25 mg/L NAC solution comprising water and an organic solvent (75:25 v/v). The results indicated the ON fluorescence intensity varied with the solvent environment. The fluorescence response is likely influenced by specific solvation and solvent–surface interactions. Among the tested solvents, the highest fluorescence recovery was observed in the presence of DMF. This behavior was consistently demonstrated through

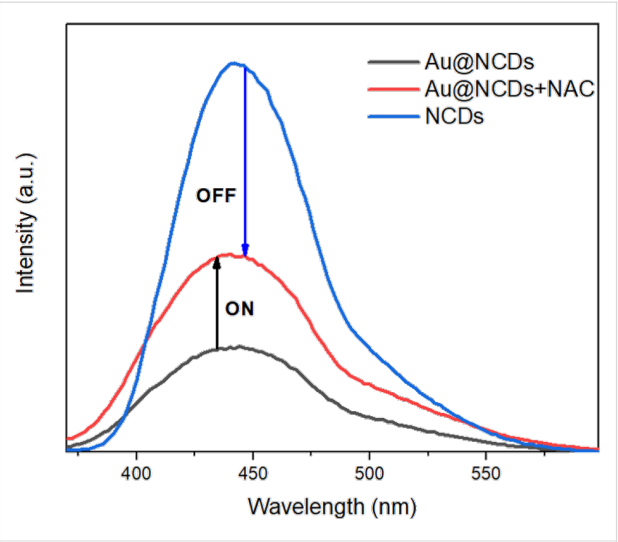

Figure 11: Photoluminescence spectra of NCDs, Au@NCDs, and Au@NCDs after adding NAC.

fluorescence measurements. To minimize the organic solvent usage in the assay, the DMF ratio was investigated across a range of 5% to 25%. As depicted in Figure 12b, a reduction in the DMF percentage led to a diminished recovered fluorescence intensity. Consequently, a DMF ratio of 25% was maintained constant throughout the study.

Spectrofluorimetric determination of *N*-acetylcysteine

As shown in Figure 13a, the fluorescence intensity of the Au@NCDs probe increased progressively with increasing NAC concentration. A good linear relationship was obtained over the concentration range of 4.0–20.0 mg/L (Figure 13b), which is described by the regression equation:

$$\Delta I = 0.8770 \times C_{\mathrm{NAC}} + 0.2068 \left(R^2 = 0.9978\right),$$

where ΔI is the fluorescence intensity change and C_{NAC} is the NAC concentration (mg/L). At concentrations higher than 20.0 mg/L, the fluorescence recovery gradually approached saturation, resulting in a reduced analytical sensitivity.

The limit of detection (LOD) and limit of quantitation (LOQ) of the proposed assay were determined based on the validated calibration range, according to the following equations:

$$\mathrm{LOD} = 3.3 \times \left(\sigma / S\right),$$

$$\mathrm{LOQ} = 10 \times \left(\sigma / S\right).$$

Here, S is the slope of the linear calibration curve, and σ represents the standard deviation of the response (ΔI). The estimated LOD and LOQ were 0.863 mg/L and 2.615 mg/L, respectively. Since the validated calibration range of the proposed method extends from 4.0 to 20.0 mg/L, the calculated LOD and LOQ should be regarded as statistical estimates of the detection and quantification capabilities based on the standard response. Reliable quantitative determination is therefore supported within the validated calibration range, while extension of the calibration curve to lower concentrations would be required to experimentally verify the practical lower limit of quantification. The analytical performance of the proposed assay is comparable to that of previously reported spectrofluorimetric methods for NAC determination [11]. Nevertheless, additional matrix-spike experiments are required for complete method validation and should be included in future studies.

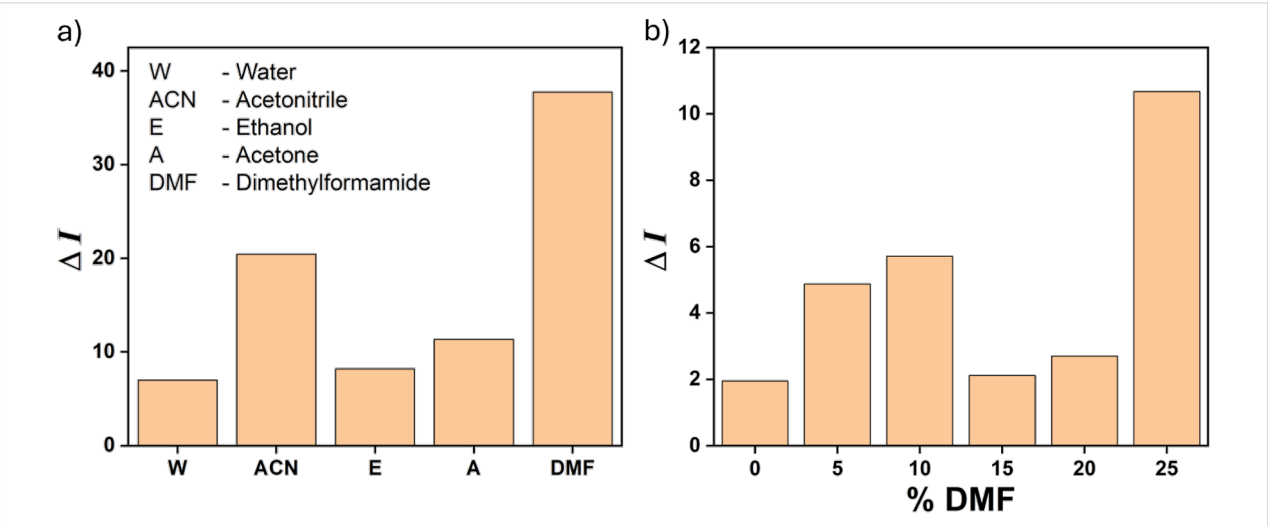

Figure 12: (a) Effect of organic solvent and (b) amount of DMF solvent ratio.

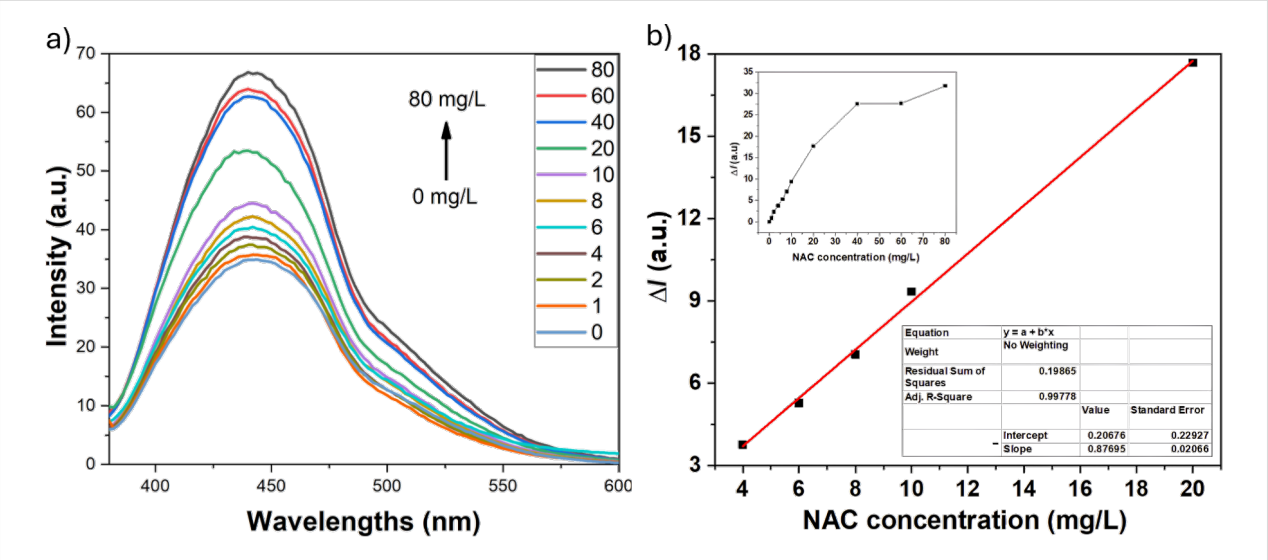

Figure 13: (a) The fluorescence spectra of Au@NCDs + NAC (0–80 mg/L); (b) calibration curve.

Conclusion

NCDs were successfully synthesized via a facile green process based on modified hydrothermal method from fresh lemon juice and urea as precursors. These NCDs function as both reducing and stabilizing agents in the subsequence synthesis of Au@NCDs. The results demonstrate the OFF–ON fluorescence behavior of the Au@NCDs in the absence and presence of *N*-acetylcysteine, a phenomenon attributed to a combination of energy transfer and ligand exchange. This proposed method holds potential for the quantitative determination of *N*-acetylcysteine.

Supporting Information

Supporting Information File 1

Additional information.
[https://www.beilstein-journals.org/bjnano/content/supplementary/2190-4286-17-75-S1.pdf]

Funding

This research is funded by the Ministry of Education and Training of Vietnam under grant number B2025-BKA-15.

Conflict of Interest

The authors declare no competing financial interests.

Author Contributions

Thuy-Huong Nguyen: data curation; formal analysis; investigation; writing – original draft. Van-Nghia Nguyen: funding acquisition; writing – original draft. Ha Thi Thu Nguyen: data curation; formal analysis; investigation; writing – original draft. Ha Ngoc Nguyen: formal analysis. Anh Duc Nguyen: data curation; formal analysis. Tuyen Viet Nguyen: data curation; formal analysis; investigation. Truong Xuan Nguyen: conceptualization; data curation; formal analysis; investigation; methodology; project administration; resources; software; supervision; validation; visualization; writing – review & editing.

ORCID® iDs

Thuy-Huong Nguyen - https://orcid.org/0009-0002-3409-6074
Van-Nghia Nguyen - https://orcid.org/0000-0001-6553-8176
Ha Thi Thu Nguyen - https://orcid.org/0000-0002-9979-2399
Ha Ngoc Nguyen - https://orcid.org/0000-0003-2480-4209
Truong Xuan Nguyen - https://orcid.org/0000-0003-0201-7212

Data Availability Statement

All data that supports the findings of this study is available in the published article and/or the supporting information of this article.

References

1. Prescott, L. F.; Ballantyne, A.; Proudfoot, A. T.; Park, J.; Adriaenssens, P. *Lancet* **1977,** *310,* 432–434. doi:10.1016/s0140-6736(77)90612-2
2. Jones, A. L. *J. Toxicol., Clin. Toxicol.* **1998,** *36,* 277–285. doi:10.3109/15563659809028022
3. Bateman, D. N.; Dear, J. W. *Toxicol. Res. (Oxford, U. K.)* **2019,** *8,* 489–498. doi:10.1039/c9tx00002j
4. Papi, A.; Alfano, F.; Bigoni, T.; Mancini, L.; Mawass, A.; Baraldi, F.; Aljama, C.; Contoli, M.; Miravitlles, M. *Arch. Bronconeumol.* **2024,** *60,* 269–278. doi:10.1016/j.arbres.2024.03.010
5. Douša, M. *J. Pharm. Biomed. Anal.* **2018,** *156,* 1–7. doi:10.1016/j.jpba.2018.04.007

6. Concha-Herrera, V.; Torres-Lapasió, J. R.; García-Alvarez-Coque, M. C. *J. Liq. Chromatogr. Relat. Technol.* **2004,** *27,* 1593–1609. doi:10.1081/jlc-120034094
7. Giljanović, J.; Brkljača, M.; Prkić, A. *Molecules* **2011,** *16,* 7224–7236. doi:10.3390/molecules16097224
8. Kukoc-Modun, L.; Radić, N. *Int. J. Anal. Chem.* **2011,** *2011,* 140756. doi:10.1155/2011/140756
9. Martinović Bevanda, A.; Arapović, A.; Vasilj, M.; Pušić, A.; Talić, S.; Ivanković, A. *Chem. Pap.* **2024,** *78,* 4261–4268. doi:10.1007/s11696-024-03386-6
10. Zhang, H.; Xu, P.; Zhang, X.; Cao, X.; Han, W.; Liu, M.; Liu, X.; Zeng, W. *Chin. Chem. Lett.* **2020,** *31,* 1083–1086. doi:10.1016/j.cclet.2019.10.005
11. Rastegarzadeh, S.; Hashemi, F. *Anal. Methods* **2015,** *7,* 1478–1483. doi:10.1039/c4ay01961j
12. Kuyumcu Savan, E. *Sens. Actuators, B* **2019,** *282,* 500–506. doi:10.1016/j.snb.2018.11.092
13. Mohammadzadeh Jahani, P.; Tajik, S.; Garkani, F. *J. Electrochem. Sci. Eng.* **2024,** *14,* 61–73. doi:10.5599/jese.2039
14. Keyvanfard, M.; Karimi-Maleh, H.; Karimi, F.; Opoku, F.; Kiarii, E. M.; Govender, P. P.; Taghavi, M.; Fu, L.; Aygun, A.; Sen, F. *Sci. Rep.* **2021,** *11,* 18060. doi:10.1038/s41598-021-97725-2
15. Hien, N. K.; Van Bay, M.; Vo, Q. V.; Ngo, S. T.; Nhan, D. T.; Nam, P. C.; Quang, D. T. *RSC Adv.* **2025,** *15,* 46925–46950. doi:10.1039/d5ra07368e
16. Mandani, S.; Sharma, B.; Dey, D.; Sarma, T. K. *Nanoscale* **2015,** *7,* 1802–1808. doi:10.1039/c4nr05424e
17. Ozyurt, D.; Al Kobaisi, M.; Hocking, R. K.; Fox, B. *Carbon Trends* **2023,** *12,* 100276. doi:10.1016/j.cartre.2023.100276
18. Pillar-Little, T. J.; Wanninayake, N.; Nease, L.; Heidary, D. K.; Glazer, E. C.; Kim, D. Y. *Carbon* **2018,** *140,* 616–623. doi:10.1016/j.carbon.2018.09.004
19. Bian, Z.; Gomez, E.; Gruebele, M.; Levine, B. G.; Link, S.; Mehmood, A.; Nie, S. *Chem. Sci.* **2025,** *16,* 4195–4212. doi:10.1039/d4sc05843g
20. Zhang, X.; Jiang, M.; Niu, N.; Chen, Z.; Li, S.; Liu, S.; Li, J. *ChemSusChem* **2018,** *11,* 11–24. doi:10.1002/cssc.201701847
21. Chen, R.; Wang, Z.; Pang, T.; Teng, Q.; Li, C.; Jiang, N.; Zheng, S.; Zhang, R.; Zheng, Y.; Chen, D.; Yuan, F. *Adv. Mater. (Weinheim, Ger.)* **2023,** *35,* 2302275. doi:10.1002/adma.202302275
22. Lan, Y.; Zhou, X.; Zheng, R.; Li, J.; Wang, M.; Wang, D.; Li, S.; Xiao, Y.; Hu, J.; Yang, M.; Li, L.; Wang, M.; Wu, J.; Gao, D. *Mater. Res. Bull.* **2026,** *194,* 113730. doi:10.1016/j.materresbull.2025.113730
23. Sahu, S.; Behera, B.; Maiti, T. K.; Mohapatra, S. *Chem. Commun.* **2012,** *48,* 8835. doi:10.1039/c2cc33796g
24. Yan, H.; Li, P.; Wen, F.; Xu, Q.; Guo, Q.; Su, W. *J. Mater. Res. Technol.* **2023,** *22,* 17–34. doi:10.1016/j.jmrt.2022.11.090
25. Ding, H.; Zhou, X.; Qin, B.; Zhou, Z.; Zhao, Y. *J. Lumin.* **2019,** *211,* 298–304. doi:10.1016/j.jlumin.2019.03.064
26. Kumawat, M. K.; Thakur, M.; Gurung, R. B.; Srivastava, R. *ACS Sustainable Chem. Eng.* **2017,** *5,* 1382–1391. doi:10.1021/acssuschemeng.6b01893
27. Khose, R. V.; Chakraborty, G.; Bondarde, M. P.; Wadekar, P. H.; Ray, A. K.; Some, S. *New J. Chem.* **2021,** *45,* 4617–4625. doi:10.1039/d0nj06259f
28. Shao, R.; Abbas, K.; Osipov, V. Y.; Zhu, H.; Li, Y.; Usama; Bi, H. *Acta Phys.-Chim. Sin.* **2026,** *42,* 100134. doi:10.1016/j.actphy.2025.100134
29. D'souza, S. L.; Chettiar, S. S.; Koduru, J. R.; Kailasa, S. K. *Optik (Munich, Ger.)* **2018,** *158,* 893–900. doi:10.1016/j.ijleo.2017.12.200
30. He, Z.; Yu, J.; Chen, X. *Alexandria Eng. J.* **2024,** *92,* 231–237. doi:10.1016/j.aej.2024.02.041
31. Munusamy, S.; Mandlimath, T. R.; Swetha, P.; Al-Sehemi, A. G.; Pannipara, M.; Koppala, S.; Shanmugam, P.; Boonyuen, S.; Pothu, R.; Boddula, R. *Environ. Res.* **2023,** *231,* 116046. doi:10.1016/j.envres.2023.116046
32. Qi, H.; Qiu, L.; Zhang, X.; Yi, T.; Jing, J.; Sami, R.; Alanazi, S. F.; Alqahtani, Z.; Aljabri, M. D.; Rahman, M. M. *RSC Adv.* **2023,** *13,* 2663–2671. doi:10.1039/d2ra07150a
33. Yuan, Z.; Hu, C.-C.; Chang, H.-T.; Lu, C. *Analyst* **2016,** *141,* 1611–1626. doi:10.1039/c5an02651b
34. Wang, Z.; Ma, L. *Coord. Chem. Rev.* **2009,** *253,* 1607–1618. doi:10.1016/j.ccr.2009.01.005
35. Lu, Z.; Giles, L. W.; Teo, B. M.; Tabor, R. F. *Colloid Interface Sci. Commun.* **2022,** *46,* 100571. doi:10.1016/j.colcom.2021.100571
36. Thakur, N.; Kandwal, P.; Pandey, R. *Ind. Eng. Chem. Res.* **2023,** *62,* 12864–12879. doi:10.1021/acs.iecr.3c01806
37. Lotfy, S.; Aboelnga, M. M.; Moawed, E. A.; Elbayoumy, E. *Nanoscale Adv.* **2026,** *8,* 2426–2449. doi:10.1039/d6na00019c
38. Liu, Y.; Cai, L.; Hao, W.; Cao, Y.; Fang, G.; Wang, S. *Food Chem.* **2026,** *517,* 149446. doi:10.1016/j.foodchem.2026.149446
39. Ma, H.-D.; Liu, J.-Y.; Chen, W.-H.; Wei, Z.; Li, Y.; Liu, Y.-F.; Du, C.-C. *J. Mol. Liq.* **2024,** *406,* 125124. doi:10.1016/j.molliq.2024.125124
40. Raji, F.; Peng, Y. *Adv. Colloid Interface Sci.* **2025,** *345,* 103644. doi:10.1016/j.cis.2025.103644
41. Fernando, A.; Aikens, C. M. *J. Phys. Chem. C* **2015,** *119,* 20179–20187. doi:10.1021/acs.jpcc.5b06833
42. Zhong, J.; Tang, X.; Tang, J.; Su, J.; Pei, Y. *J. Phys. Chem. C* **2015,** *119,* 9205–9214. doi:10.1021/jp511615r
43. Haque, M. H.; Koh, K.; Sohn, H. *Macromolecules* **2023,** *56,* 6396–6406. doi:10.1021/acs.macromol.2c02193
44. Fu, C.; Feng, X.; Tian, H.; Zhang, Y.; Zhai, Z.; Qiu, P.; Hu, C.; Liu, J.; Wang, J. *Appl. Surf. Sci.* **2025,** *702,* 163380. doi:10.1016/j.apsusc.2025.163380
45. Ha, N. T. T.; Thao, V. T.; Ha, N. N. *Photochem. Photobiol. Sci.* **2026,** *25,* 1035–1047. doi:10.1007/s43630-026-00900-5
46. Wang, S.; Huo, X.; Zhao, H.; Dong, Y.; Cheng, Q.; Li, Y. *Chem. Phys. Impact* **2022,** *5,* 100112. doi:10.1016/j.chphi.2022.100112
47. Hinterberger, V.; Damm, C.; Haines, P.; Guldi, D. M.; Peukert, W. *Nanoscale* **2019,** *11,* 8464–8474. doi:10.1039/c9nr01029g
48. Oliveira, A. E. F.; Pereira, A. C.; Resende, M. A. C.; Ferreira, L. F. *Analytica* **2023,** *4,* 250–263. doi:10.3390/analytica4020020
49. García, A.; Papior, N.; Akhtar, A.; Artacho, E.; Blum, V.; Bosoni, E.; Brandimarte, P.; Brandbyge, M.; Cerdá, J. I.; Corsetti, F.; Cuadrado, R.; Dikan, V.; Ferrer, J.; Gale, J.; García-Fernández, P.; García-Suárez, V. M.; García, S.; Huhs, G.; Illera, S.; Korytár, R.; Koval, P.; Lebedeva, I.; Lin, L.; López-Tarifa, P.; Mayo, S. G.; Mohr, S.; Ordejón, P.; Postnikov, A.; Pouillon, Y.; Pruneda, M.; Robles, R.; Sánchez-Portal, D.; Soler, J. M.; Ullah, R.; Yu, V. W.-z.; Junquera, J. *J. Chem. Phys.* **2020,** *152,* 204108. doi:10.1063/5.0005077
50. Perdew, J. P.; Burke, K.; Ernzerhof, M. *Phys. Rev. Lett.* **1997,** *78,* 1396. doi:10.1103/physrevlett.78.1396
51. Ehlert, S. *J. Open Source Software* **2024,** *9,* 7169. doi:10.21105/joss.07169
52. Grimme, S.; Hansen, A.; Brandenburg, J. G.; Bannwarth, C. *Chem. Rev.* **2016,** *116,* 5105–5154. doi:10.1021/acs.chemrev.5b00533

53. Hieu, N. H.; Huyen, N. T.; Thoai, N. D.; Ha, N. N.; Ha, N. T. T. *J. Nanopart. Res.* **2026,** *28,* 49. doi:10.1007/s11051-026-06567-4
54. Tran, T.-Q.; Tran, H.-M.; Nguyen, X.-T.; Nguyen, D.-T.; Giang, P.-L. T.; Nguyen, N.-T. *Top. Catal.* **2023,** *66,* 104–116. doi:10.1007/s11244-022-01732-0
55. Nguyen, N. T.; Nguyen, X. T.; Nguyen, D.-T.; Tran, H. M.; Nguyen, T. M.; Tran, T. Q. *Adsorpt. Sci. Technol.* **2021,** *2021,* 5906248. doi:10.1155/2021/5906248
56. Simões, E. F. C.; Leitão, J. M. M.; da Silva, J. C. G. E. *Microchim. Acta* **2016,** *183,* 1769–1777. doi:10.1007/s00604-016-1807-6
57. Li, X.; Hu, Q.; Yang, K.; Zhao, S.; Zhu, S.; Wang, B.; Zhang, Y.; Yi, J.; Song, X.; Lan, M. *Sens. Actuators, B* **2022,** *371,* 132534. doi:10.1016/j.snb.2022.132534
58. Qin, X.; Lu, Y.; Bian, M.; Xiao, Z.; Zhang, Y.; Yuan, Y. *Anal. Chim. Acta* **2019,** *1091,* 119–126. doi:10.1016/j.aca.2019.09.031
59. Vervald, A. M.; Laptinskiy, K. A.; Chugreeva, G. N.; Burikov, S. A.; Dolenko, T. A. *J. Phys. Chem. C* **2023,** *127,* 21617–21628. doi:10.1021/acs.jpcc.3c05231
60. Korram, J.; Dewangan, L.; Nagwanshi, R.; Karbhal, I.; Ghosh, K. K.; Satnami, M. L. *New J. Chem.* **2019,** *43,* 6874–6882. doi:10.1039/c9nj00555b
61. Kim, N.; Lee, J.; Gu, M.; Kim, B.-S. *Carbon Energy* **2021,** *3,* 590–614. doi:10.1002/cey2.115

License and Terms